Detection of Biomarkers for Lung Cancer and Leukemia using SPR Nanohole-Based Sensors

by

Ting Yu
B.Sc., University of Victoria, 2008

A Thesis Submitted in Partial Fulfillment
of the Requirements for the Degree of

MASTER OF SCIENCE

in the Department of Chemistry

Supervisory Committee

Detection of Biomarkers for Lung Cancer and Leukemia using SPR Nanohole-Based Sensors

by

Ting Yu
B.Sc., University of Victoria, 2008

Supervisory Committee

Dr. Alexandre G. Brolo, (Department of Chemistry)
Supervisor

Dr. Dennis Hore, (Department of Chemistry)
Departmental Member

Dr. Tom Fyles, (Department of Chemistry)
Departmental Member

Abstract

Supervisory Committee
Dr. Alexandre G. Brolo, (Department of Chemistry)
Supervisor
Dr. Dennis Hore, (Department of Chemistry)
Departmental Member
Dr. Tom Fyles, (Department of Chemistry)
Departmental Member

Cancer is a leading cause of death and some types of cancer are hard to diagnose at early stages. An accurate method for subtype classification of cancer types is also critical for patients to receive effective treatments. Many cancer biomarkers (e.g., EGFR for lung cancers and CD19/CD20 for leukemia) have been found with potential of being used for cancer diagnosis and subtype cancer classification. A biosensing technique being able to detect biomarkers with a miniaturized system, based on extraordinary light transmission (EOT) through nanohole arrays on metal films, is promising for cancer diagnosis and subtype classifications. In this research, the detection of different biomarkers (EGFR, CD19 and CD20) was demonstrated using a surface plasmon resonance (SPR) setup with EOT. The concentration of EGFR from cell lysate solution was determined using the SPR setup and compared with a current analytical method (ELISA). The SPR setup gave a detection limit concentration of 0.77 μg/mL for the EGFR. The EGFR concentration from the cell lysate was determined to be greater than 10 μg/mL from SPR experiments; while a lower concentration of 0.604 μg/mL was found from ELISA indicating some problems with the calibration curves obtained in the SPR experiments. A whole lung cancer cell capture experiment was also conducted using

microscopy imaging and the SPR setup. A number of 11 ± 2 cells/mm^2 was captured from a pre-modified metal surface, which was confirmed by SPR.

Table of Contents

List of Tables

List of Figures

List of Abbreviation

AP	Alkaline phosphatase
BSA	Bovine serum albumin
CAD	Computer-aided design
CEA	Carcinoembryonic antigen
CLL	Chronic lymphocytic leukemia
DMEM	Dulbecco's Modified Eagle Medium
EDC	1-ethyl-3-(3-dimethylaminopropyl)carbodiimide
EGF	Epidermal growth factor
EGFR	Epidermal growth factor receptor
ELISA	Enzyme linked immunosorbent assay
EOT	Extraordinary optical transmission
FIB	Focused ion beam
HRP	Horseradish peroxidase
IL	Interference Lithography
MIA	Magnetic immunoassay
MRI	Magnetic resonance imaging
NHS	N-hydroxysuccinimide
NP40	Nonidet-P40
NSCLC	Non-small cell lung cancer
PBS	Phosphate buffered saline
PDMS	Polydimethylsiloxane
PEG	Polyethylene glycol
PET	Positron emission tomography
RIA	Radioimmunoassay
SDS	Sodium Dodecyl Sulfate
TMB	Tetramethylbenzidine

Acknowledgments

I acknowledge, with greatest appreciation, to my supervisor, Dr. Alexandre Brolo for his guidance and help through my graduate research. I would also like to thank all the past and present group members for the support and inspiration, Mohammad Rahman and Jacson Menezes for nanohole sample fabrication, Carlos Escobedo for the PDMS making, Rob Sahota from the BCCA-Vancouver Island Centre for the cell line, and Dr. Jeremy Wulff for providing the facility to grow the cell. And finally, I acknowledge my family for their support and understanding during those weekends I spent in the lab.

Chapter One : Introduction

1.1 Ultimate Goal

Cancer is a leading cause of death in Canada with an estimated 186,400 new cases and 75,700 deaths from cancer in 2012[1]. More than 200 types of cancers are found based on the current cancer classification. In order for a patient to receive appropriate therapy treatment, the cancer type must be identified as accurately as possible by the clinician, and also at a relatively early stage for higher survival rate[2,3]. However the morphological inspection is still the standard diagnostic method, which is not the best option for early cancer diagnosis and gives limited information of the cancer such as rate of proliferation, capacity of invasion, and resistance mechanism to certain treatment agents[2]. Therefore a molecular method looking for the DNA, RNA or protein of a defined marker that is correlated to a certain subtype of cancer and possibly being used for early cancer diagnosis is needed[4,9]. The ultimate goal of this research is to help developing a label free biosensor that is able to detect cancer markers from physiological fluids, such as cell lysate from biopsied samples or blood, for early cancer diagnosis and helping to classify cancer subtypes for patients to receive efficient and accurate treatment.

In an ideal scenario, blood samples or biopsied samples are collected from a patient. The raw sample is then introduced to a miniaturized device that contains a biosensor and a microfluidic system[5]. After passing through on chip sample preparation stages, the fluid is introduced into a detection chamber, where calibrations of different protein biomarkers correlate to the cancer of interest could be run to quantify the level of the biomarkers in the sample. Based on the level of the biomarkers determined from the

device, two outcomes should be determined: the risk level of the patient and/or the subtypes of the cancer. Based on the results, the patient could be sent for further tests if in low risk or to more comprehensive examinations and receive appropriate treatments[13,14] if in high risk. The device should be portable and easy-to-use for the requirement of screening a large number of patients efficiently in clinical settings.

1.2 Thesis Goal

In order to achieve the ultimate goal as stated in section 1.1, our research group has been working on developing a biosensing device based on the optical properties of nanohole arrays on gold thin films in transmission mode. The theory behind the detection method is based on the excitation of surface plasmon resonance (SPR) at the interface of the metal that enhances the transmission of light at certain wavelengths. Previous experiments on SPR sensing of proteins with nanohole arrays have been reported[6]. In this thesis, we implement the nanohole SPR sensing method to applications related to different protein biomarkers for both lung cancer and leukemia. By performing a calibration curve from the biomarkers, the amount of biomarkers in lung cancer cells was quantified, and compared with ELISA (a commercially available biosensing methodology). The method was evaluated in terms of sensor resolution, sensitivity, and detection limit.

1.3 Why Lung Cancer and Leukemia?

Lung cancer was chosen for our first step target because it is the leading cause of cancer deaths in North America and worldwide for both men and women[7]. Because lung cancer is hard to be detected at early stage, its mortality rate remains the highest in North America[8]. According to the estimation from Canadian Cancer Society, there are 25,600 new cases and 20,100 deaths in lung cancers in Canada in 2012[1]. Most patients with lung cancer being diagnosed are not curable, and the 5-year survival rate for all patients is less than 10%[9]. However studies have shown that the 5-year survival rate increases to greater than 90% if the cancer is found at early stage and followed with proper treatment[10]. Therefore, a biosensing device that could be used for screening of lung cancer may be helpful to improve the disease curability and patient survival rate.

In order to prove that the biosensing device should work for any type of cancers, leukemia was chosen as our second target. Comparing to lung cancers, the death rate of leukemia is not as high (an estimation of 5,600 new cases and 2,600 deaths in Canada in 2012[1]); however it is still the sixth leading cause of cancer death in men and seventh leading cause of cancer death among women in Canada[1]. Test is relatively easy to perform for leukemia by counting blood cells through screening peripheral blood examination[9]. Nevertheless take chronic lymphocytic leukemia (CLL) for example, the definition of lymphocytosis in CLL varies from 5×10^9/L to 15×10^9/L, of which most cells are small and indistinguishable mature-appearing lymphocytes[11, 12]. This introduces difficulties for the precise type determination of CLL (in order for the patient to undergo further diagnosis and receive effective treatment)[13]. With an abundant number of biomarkers available for leukemia studies, cell surface biomarkers analysis is clearly

helpful in making a specific diagnosis of leukemia[13]; therefore the detection of biomarkers for leukemia using the biosensing device could be a good candidate for screening of leukemia subtype classification.

1.4 Current Diagnosis Methods for Lung Cancers

Lung cancer diagnosis is a variable process, which is done depending on factors such as patient medical history, symptoms and findings on physical examinations[14]. The most common diagnosis methods include laboratory testing, imaging tests, and tissue diagnosis. Although there are a variety of techniques to assist physicians in obtaining an accurate diagnosis, no single test could reliably identify lung cancer at early stages[15].

When a patient is suspected with symptoms of lung cancer, laboratory testing is usually included in the diagnostic work-up. Sputum cytology and CEA (carcinoembryonic antigen) test are the most common stained and examined diagnosis methods performed. For the sputum cytology test, the sputum collected from a patient, is examined under a microscope. Cancer cells that may be contained in the sputum are visually identified[14]. However the detection rate of lung cancers with sputum cytology can be as low as 5-20%[16,17]. Another test is sometimes performed is the detection of CEA, a tumor marker that is found in blood when cancer is present. However, CEA is found overexpressed in several cancers, which does not necessarily indicate specifically lung cancer[14].

Imaging tests such as Chest X-Rays, CT scans (computerized tomographic scans), MRI (magnetic resonance imaging) and PET (positron emission tomography) scans are tests that can be performed to determine if a lung tumor is present and likely to be benign

or malignant[14]. These tests are useful to look for enlarged lymph nodes indicating cancerous spread; yet these tests are complex and highly rely on the experience of Oncologist[18].

Tissue diagnosis is currently the only way to make a clear diagnosis of the type and stage of lung cancer present[14]. By obtaining a tissue sample (biopsy) from a patient's lung, the type and stage of the cancer is determined by the Oncologist using a regular optical microscope. Bronchoscopy is the most common technique to examine tissue biopsys from the lungs by using a small and flexible tube through the airways of the lungs[14]. Tissue diagnosis also requires a lot of experience from pathologists in order to obtain an accurate diagnosis, and they are not suitable for cancer screening.

Although screening with sputum cytology and routine chest radiology have been assessed, no major organization currently recommends lung cancer screening considering its cost-effectiveness and high false-positive rates[19]. Scientists are working hard to find more biomarkers that are sensitive and specific for lung cancers. A technique that could effectively detect several biomarkers and be cost saving is then desperately needed for lung cancer screening.

1.5 Current Diagnosis Methods for Leukemia

The most common diagnosis procedures for leukemia are complete blood cell count and morphologic assessment of peripheral blood, morphologic examination of bone marrow biopsy, cytogenetics and immunophenotyping (i.e. FISH, fluorescence microscopy and flow cytometry)[13]. Compared to lung cancer diagnosis, leukemia is relatively easy to be screened by simply obtaining a blood sample from the patient and

count the number of white blood cells in it. However, in order to receive effective and specific therapeutic treatment, the type of leukemia has to be accurately identified, which cannot be achieved by just white blood cell counting[9].

Morphological assessment of normal and abnormal cell components of peripheral blood and bone marrow remains the essential diagnosis tool to classify hematologic malignant diseases. By examine the blood or marrow smear under microscope, the nature of the disease and requirement of specific treatment can often be determined[13]. However, this requires extensive experiences from doctors, and is not suitable for screening of a large number of patients for leukemia classifications.

Cytogenics identify specific chromosome abnormalities relating to certain types of leukemia; immunophenotyping detects different biomarker antigens react with specific antibodies that are overexpressed in different types of leukemia. Both methods are critical for the diagnosis of leukemia, and useful for classification of the subtypes. However these techniques require labelling of the sample with fluorophores or other kind of labels[20,21], which complicates the use of the techniques for screening purposes.

During the past 20 years, many antibodies specific to different CD (cluster of differentiation) biomarkers have become available [22, 23], which are useful for the classification of leukemia. An easy-to-use, label-free and cost-effective biosensing technique that can detect multiple biomarkers in real time would play an increasing role in in the future of leukemia diagnosis.

1.6 Biomarkers

According to the Encyclopedic Reference of Cancer, biomarkers are parameters that can provide information about the expression and state of a disease[24]. For our project, the biomarkers are the cell surface proteins that are overexpressed in lung cancer or leukemia cells, which can be used to diagnosis the diseases. There are a few markers found for lung cancer and many for leukemia[9,25,26]. We chose EGFR (epidermal growth factor receptor) for the lung cancer study and CD19 and CD20 for the leukemia study. A detailed description of the biomarkers will be discussed in Chapter Two.

1.7 Structure of the Thesis

This thesis is divided into seven chapters. A general introduction of the motivation and the goals of the thesis are provided in Chapter One. Chapter Two provides the theory of SPR and information about the immune system, which are the foundation of our research. The fabrication methods are described in Chapter Three. The experimental details were concluded in Chapter Four. Chapter Five shows the experimental results of the detection of EGFR, CD19 and CD20 biomarkers using SPR nanohole arrays. The possibility of captures single lung cancer cells and imaging following the same experimental procedure of SPR experiment is discussed in Chapter Six with the preliminary results presented there. All results are summarized in Chapter Seven.

Chapter Two : Background

2.1 Surface Plasmon Resonance (SPR)

2.1.1 History

In 1902, Wood documented the first observation of surface plasmons[27]. He observed unevenly distributed spectra formed by a diffraction grating of polychromatic light, which he could not explain[27]. Based on theoretical considerations, Fano concludes that Wood's observations were connected with the excitation of electromagnetic waves on the surface of the grating[28]. Some fifty years later, in 1956, Pines theoretically described the energy loss by electrons travelling through metal due to collective oscillations of free electrons; he called these oscillations Plasmons[29]. One year later, a study was published by Ritchie, in which it was shown that plasmon modes can exist near the surface of metal[30]. This study represents the first theoretical explanation of surface plasmons. In 1968, about seventy years later after Wood's first observations, Ritchie and his coworkers described the anomalous spectrum behaviour of metal gratings as the excitation of surface plasmon resonance on the grating[31]. In the same year, Kretschmann and Raether presented another method, based on the attenuated total reflection, for the optical excitation of surface plasmons on metal films[32]. In Kretschmann's setup, a thin metal film was deposited on a supporting glass prism without gap, and the surface plasmons were excited from the other side of the metal surface[33]. This configuration has been widely used in many practical applications for biomolecule or environment studies[34]. In 1990, the first SPR-based analytical instrument for biomolecular interaction studies was

developed (Biacore)[35]. Since then, SPR techniques have been applied to many fields of study[34,36].

2.1.2 SPR Sensors

Surface plasmons were widely accepted in surface science following the pioneering work of Ritchie[31]. Surface plasmons are electromagnetic waves that propagate along a metal-dielectric interface. They are basically light waves trapped at the surface of the metal[37]. One of the most attractive aspect of surface plasmons is that they concentrate light leading to electric field enhancement, which can be used to monitor light-matter interactions and suitable for sensor applications[38].

In SPR sensors, a surface plasmon is excited at a metal-dielectric interface, where changes in refractive index are measured. A change in refractive index of the dielectric medium produces a change in propagation constant of the surface plasmon, which affects the coupling conditions between the optical wave and surface plasmon; this coupling condition change can be observed as one of the changes in angles, wavelength, intensity, phase or polarization of the light wave interacting with the surface plasmon[39]. SPR sensors can be classified based on which of the characteristic changes is measured.

SPR sensors can also be direct or indirect based on which quantity is measured. In direct SPR sensors, refractive index is determined based on the sensor output (angle, wavelength, intensity, phase or polarization). In indirect SPR sensors, the measurement is usually a concentration of a chemical or biological analyte through binding of the analyte to a specific element at the interface surface, which converts into a refractive index

change. The SPR affinity biosensor is a typical indirect SPR sensor that is commonly used in biosensing studies[39].

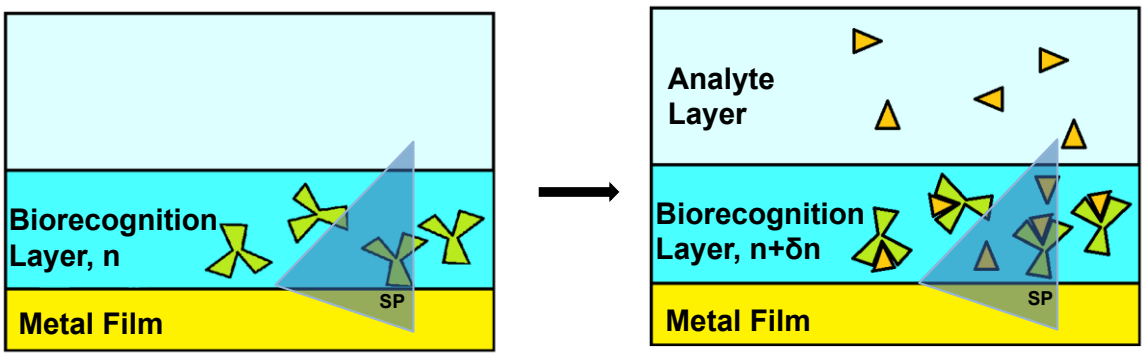

Figure 2-1: Principle concept of SPR affinity biosensor, the blue triangle represents the field of surface plasmon.

As shown in Figure 2-1, in a SPR affinity biosensor, the biorecognition element (e.g. antibody) is first immobilized on the surface of a metal film. When a solution containing the analyte of interest (e.g. antigen specific to the antibody) is introduced to the sensor surface, analyte molecules bind to the biorecognition element, resulting in an increasing in refractive index at the interface, which is determined by one of the characteristics of optical wave interacting with the surface plasmon at the sensor surface. The amount of the refractive index change due to the binding depends on the structure of the analyte molecule and the surface concentration of the analyte; and it can be described from the equation below:

$$\Delta n = \left(\frac{dn}{dc}\right)\frac{\Gamma}{h} \quad \textbf{(2-1)}$$

where Δn is the amount of refractive index change, $\frac{dn}{dc}$ the volume refractive index increment, h the sensor surface thickness, and Γ the surface concentration in mass/area[40].

2.1.3 Resonance Conditions for Surface Plasmon

The propagation constant of the surface plasmon wave at the dieletric-metal interface is given by the following equation:

$$\boldsymbol{\beta = k\sqrt{\frac{\varepsilon_m n_s^2}{\varepsilon_m + n_s^2}}} \qquad \textbf{(2-2)}$$

where k is the free space wave number, ε_m the complex dielectric constant of the metal ($\varepsilon_m = \varepsilon_{mr} + i\varepsilon_{mi}$), and n_s the refractive index of the dielectric[38].

In order to fulfill the condition for surface plasmon, the material used has to have the condition of $\varepsilon_{mr} < -n_s^2$, which can be satisfied by several metals such as silver and gold[41]. However due to the high loss from adsorption in metal, the propagation length of the surface plasmon wave is limited to μm range; the surface plasmon field, which is perpendicular to the surface, also decays exponentially as the distance from the metal increases[38]. Therefore in order to generate surface plasmon for sensing actions, the interaction resulting from the refractive index change has to be directly in the area where surface plasmon is excited by an optical wave[59].

As follows from equation 2-2, the propagation constant of surface plasmon is always greater than that of the incident optical wave, which could not excite surface plasmon directly at the metal-dielectric interface. If somehow we could increase the

momentum of the incident optical wave at the metal-dielectric interface, and match with the momentum of surface plasmon at the resonance frequency, the surface plasmon then can be excited. The excitation of surface plasmon by optical wave will result in the energy from the optical wave absorbed to generate surface plasmons; and because of the high concentration of the electromagnetic field at the surface, the SPR condition is very sensitive to changes in the optical properties at the dielectric-metal interface[42]. The increase of optical wave momentum at the dielectric-metal interface is commonly achieved by prism coupling, grating coupling and waveguide coupling[42]. The detailed mechanism of the prism coupling and grating coupling configurations will be discussed in this chapter.

2.1.4 Prism Coupling

The most common method of excitation of surface plasmons is by coupling with a prism, and the Krestcshmann configuration is the most commonly used prism coupling setups in many SPR systems reported to date[42].

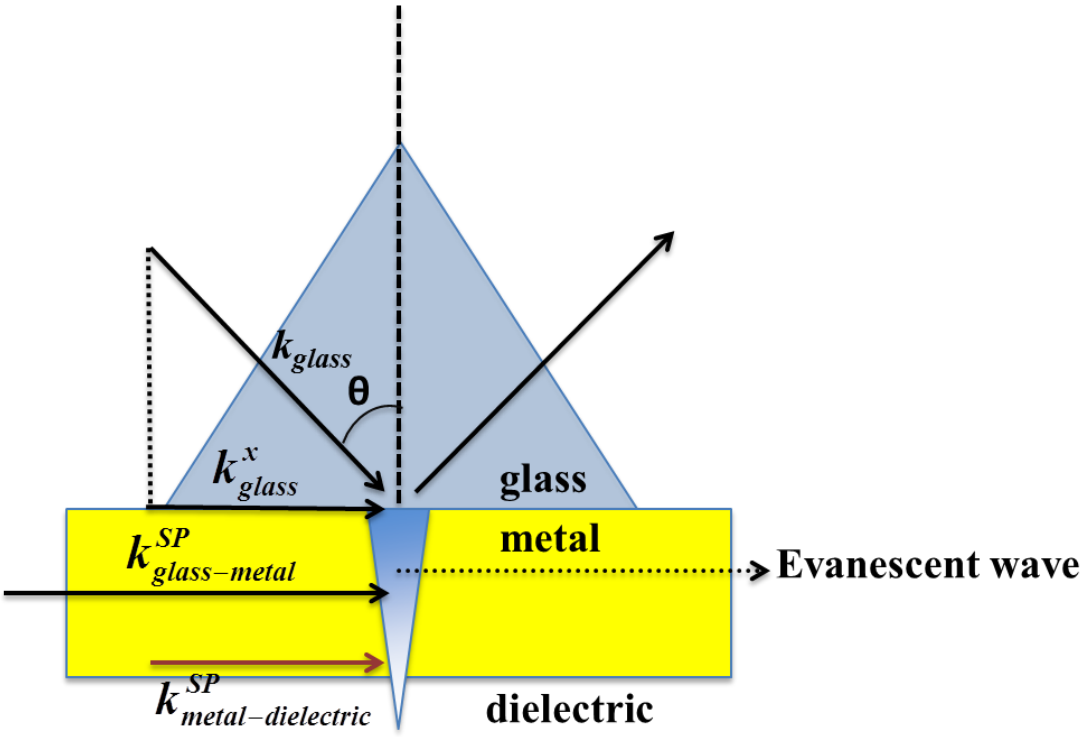

Figure 2-2: Schematic illustration of the momentum for the Au-glass and Au-air interface of the Kretschmann configuration, where surface plasmons are excited by prism-coupling.

As shown in Figure 2-2, in the Kretschmann setup, a high refractive index prism is interfaced with a metal-dielectric waveguide consisting of a thin layer of metal film (about 50 nm for visible light)[39]. When light propagating in the prism illuminates the metal at an incident angle θ, the parallel component of the incident light momentum, k^{x}_{glass}, can be expressed as in equation 2-3. The surface plasmon momentum at the glass-metal interface, $k^{SP}_{glass-metal}$, can be determined using the dielectric constants of the glass and the metal (ε_{glass} and ε_{metal}) as shown in equation 2-4[39]. At all incident angles, $k^{SP}_{glass-metal}$ is always greater than k^{x}_{glass}. Therefore, the SPR condition cannot be met at the glass-metal interface[42].

$$k_{glass}^{x} = k_{glass}\sin\theta \quad \textbf{(2-3)}$$

$$k_{glass-metal}^{SP} = k_{glass}\sqrt{\frac{\varepsilon_{glass}\varepsilon_{metal}}{\varepsilon_{glass}+\varepsilon_{metal}}} \quad \textbf{(2-4)}$$

However, when the incident angle is greater than the critical angle, part of the light travels through the thin metal layer and generates an inhomogeneous wave that decays exponentially in the direction perpendicular to the prism-metal interface. This wave is referred as an evanescent wave as shown in Figure 2-2. In this case, the surface plasmon momentum at the metal-dielectric interface, $k_{metal-dielectric}^{SP}$, is given by equation 2-5. Meanwhile, the evanescent wave carrying the same character as the incident light can have a momentum matched with $k_{metal-dielectric}^{SP}$ at certain incident angle, which excites the surface plasmon on the metal-dielectric side. This angle is called SPR angle[42].

$$k_{metal-dielectric}^{SP} = k_{dielectric}\sqrt{\frac{\varepsilon_{dielectric}\varepsilon_{metal}}{\varepsilon_{dielectric}+\varepsilon_{metal}}} \quad \textbf{(2-5)}$$

2.1.5 Grating Coupling

Another approach to optically excite surface plasmon is based on the diffraction of light on a metallic grating[42]. A metallic grating can be fabricated by making a periodic pattern of metallic nanoparticles or lines, and nanoholes on a metal surface[39,43]. As shown in Figure 2-3, when an incident light strikes on a gold (metal) grating surface, surface plasmon can be excited directly by grating coupling[42]. Similar to the discussion in section 2.1.4, the parallel component of the incident light momentum, k_x, has to match the

surface plasmon momentum, k_{SP}, in order to meet the SPR condition. This is expressed in the equation 2-6 as shown below:

$$\boldsymbol{k_x = \left(\frac{\omega}{c}\right)\sin\theta \pm \frac{2\pi}{\Lambda} m = k_{SP}} \quad \textbf{(2-6)}$$

where ω is angular frequency, c the speed of light, m the integer, and Λ the periodicity of array. The integer m gives multiple values for k_x, and one of them would match k_{SP} at a certain angle θ. Surface plasmon can be excited without a prism in this case as the value of k_x could change depending on both the incident angle and the periodicity of array.

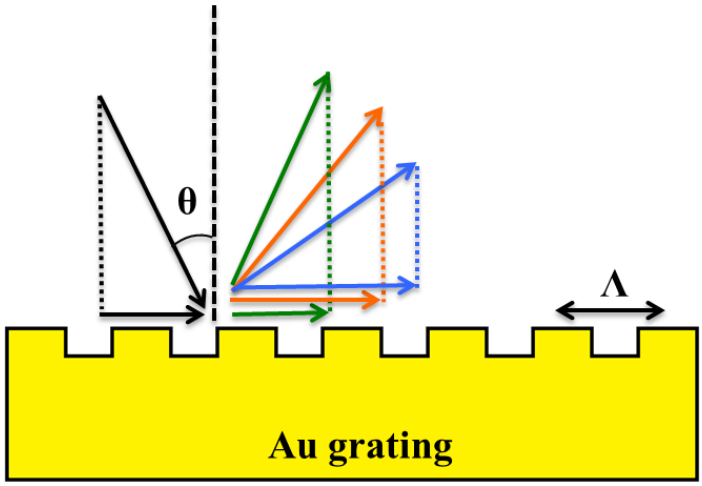

Figure 2-3: Schematic illustration of the surface plasmon resonance excited by grating-coupling, where the incident light momentum matches the surface plasmon momentum at certain incident angle and periodicity of the arrays.

2.1.6 Extraordinary Optical Transmission

In 1944, Bethe theoretically showed that the transmission efficiency of light through a single subwavelength hole on an infinitely thin and perfect metal decreases with the ratio of the hole radius and wavelength to the fourth power[43]. However, for real metal with a finite thickness, an extraordinary optical transmission (EOT) of light was observed through arrays of subwavelength holes in silver and gold films by Ebbesen in 1998[59].

Figure 2-4 demonstrates the enhanced transmission of light by EOT. When an incident light is shining through the arrays of holes with subwavelength aperture, the transmitted light at certain wavelength is greatly enhanced, and this effect of increasing light transmission is due to coupling of light with the surface plasmon resonance (grating coupling). As mentioned in section 2.1.3, surface plasmon waves propagate parallel to the metal-dielectric surface and they are confined within the area adjacent to the surface. The periodicity of the arrays determined the transmission peak position, and the sharpness of the peak is determined by geometric parameters, such as hole size and film thickness, and by the roughness of the metal film[49]. By modifying metallic nanostructures, the enhancement of the light transmitted can be manipulated within different wavelength ranges.

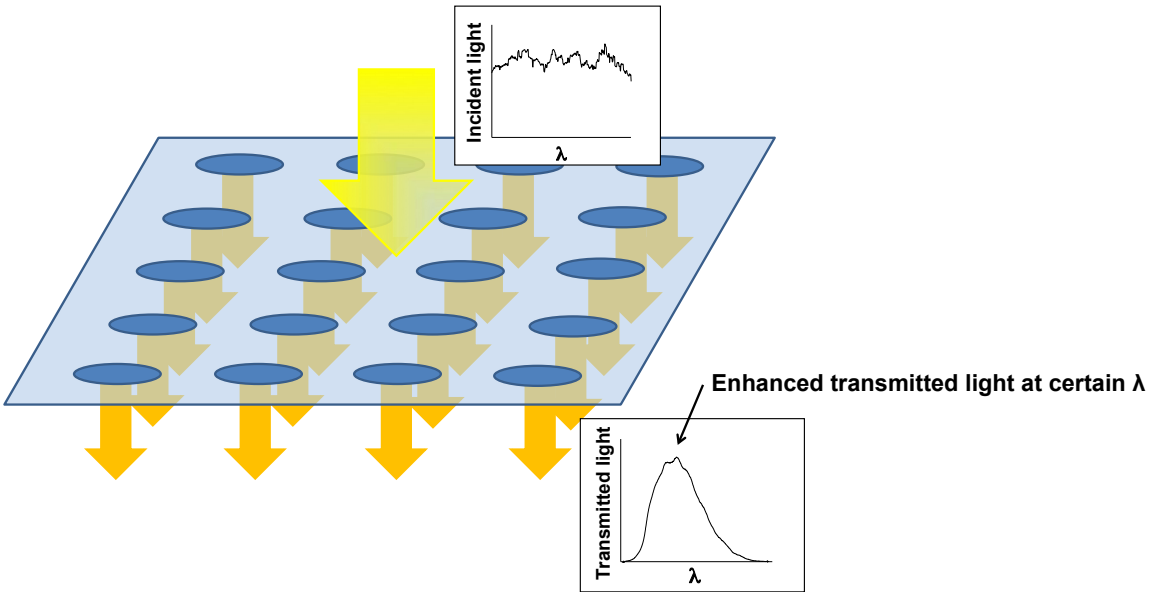

Figure 2-4: Enhanced transmitted light at certain wavelengths through sub-wavelength nanohole arrays. This phenomenon is called extraordinary optical transmission (EOT).

2.1.7 Principle of EOT Biosensing

SPR biosensing can be realized using a thin layer of gold film with a periodic nanohole array structure. In a typical experiment, while light is incident to the array at normal illumination and the enhanced transmitted light spectrum (with resonance peaks due to EOT and grating coupling SPR) is measured. The SPR condition for grating coupling is satisfied by equation 2.6. In the case of a 2D grating, the equation is modified as shown below:

$$k_x = \left(\frac{\omega}{c}\right)\sin\theta \pm \frac{2\pi}{\Lambda}\sqrt{i^2 + j^2} = k_{SP} = \frac{2\pi}{\lambda}\sqrt{\frac{\varepsilon_{gold}\varepsilon_{dielectric}}{\varepsilon_{gold}+\varepsilon_{dielectric}}} \qquad (2\text{-}7)$$

Because the transmission light is at normal incident, $\sin\theta$ equals to zero. The equation above can then be simplified and rearranged to equation 2-8:

$$\boldsymbol{\lambda = \Lambda\sqrt{(i^2 + j^2)^{-1}}\sqrt{\frac{\varepsilon_{gold}\varepsilon_{dielectric}}{\varepsilon_{gold}+\varepsilon_{dielectric}}}} \qquad \textbf{(2-8)}$$

where λ is the wavelength of the transmitted light, Λ the periodicity of the array, ε_{gold} and $\varepsilon_{dielectric}$ the dielectric constants of the gold and the dielectric layer, and *i* and *j* the integers defining the arrays' scattering order along the x and y directions, respectively.

As can be seen from equation 2-8, the SPR resonance wavelength of the transmitted light depends on the periodicity of the nanohole array structure and on the dielectric conditions at the gold- interface (dielectric constants of gold and dielectric layer). With fixed periodicity, the SPR resonance wavelength of the transmitted light will change in response to the changes in surface condition (for instance, molecular absorption to the metal-dielectric interface).

2.2 Immunoassays

Immunoassays have been commonly used in biological research to determine the concentrations of analytes in biological fluid and in the investigation of the physiological and pathological role of different substances that are biologically active (e.g. for the identification of therapeutic targets or biomarkers)[44]. The principle of immunoassays involves a protein molecule (antibody or antigen) that binds specifically to the analyte of interest (antigen or antibody). Because antibodies possess high specificity and affinity

towards their antigens, immunoassays are specific and highly selective[44]. Another feature of typical immunoassays is the involvement of a detectable label (i.e. radioactive elements, enzymes, dyes and etc.) in order to produce a measurable signal in response to a specific binding. Different methods of immunoassays have been developed based on the type of labels and number of antibody or antigen used in the test. The common methods include enzyme-linked immunosorbent assay (ELISA), magnetic immunoassay (MIA) and radioimmunoassay (RIA). ELISA was used in our experiments to determine and compare the analyte concentration with the SPR sensor that we developed. A detailed description of ELISA is introduced in the following section.

2.2.1 ELISA

ELISA is the most common immunoassay technique for antigen quantitation and antibody detection[45]. The fundamental principle of ELISA is the use of an enzyme coupled with antibodies or antigens. The enzyme-labeled protein is used to detect the species of interest. The enzyme catalyzes the formation of products that can be optically detected, such as a colour change or a fluorescence emission. A calibration curve is generated by measuring the optical property at different concentrations of standards with known concentrations of the species of interest. The result from the unknown sample is interpolated into a standard curve, and the concentration of the substrate is determined[45]. The common enzymes used for ELISA are horseradish peroxidase (HRP) and alkaline phosphatase (AP) [46].

There are different types of ELISA assays based on how the ultimate detection is carried out. One of the most common formats is the sandwich assay ELISA. This method involves the capturing of the antigen of interest between two primary antibodies: the

capture antibody and the detection antibody. High selectivity is one of the main advantages of sandwich assay ELISA, because two primary antibodies are used[46]. A scheme of the sandwich method for ELISA is shown in Figure 2-5. First, primary antibodies (capture antibodies) are absorbed to the inner surface of a well in a polystyrene plate. A solution of nonspecific proteins, such as bovine serum albumin (BSA), is then added to block any surface that is not coated by the capture antibody. This step will eliminate the unspecific bindings of antibody or antigen introduced to the surface. Next, the sample is added, and the analyte of interest (antigen in this case) binds specifically to the primary (capture) antibody. Unbounded antigen is washed away, and another primary antibody (detection antibody) is added afterwards, forming a sandwich format. Finally, the enzyme-linked secondary antibodies are added, which also specifically bind to the primary (detection) antibody. A substrate (specific to the enzyme) is added later on, and the reaction between the substrate and the enzyme takes place forming, for instance, a colored product. Product formation (monitored as color intensity) is proportional to the concentration of the antigens in the sample[47].

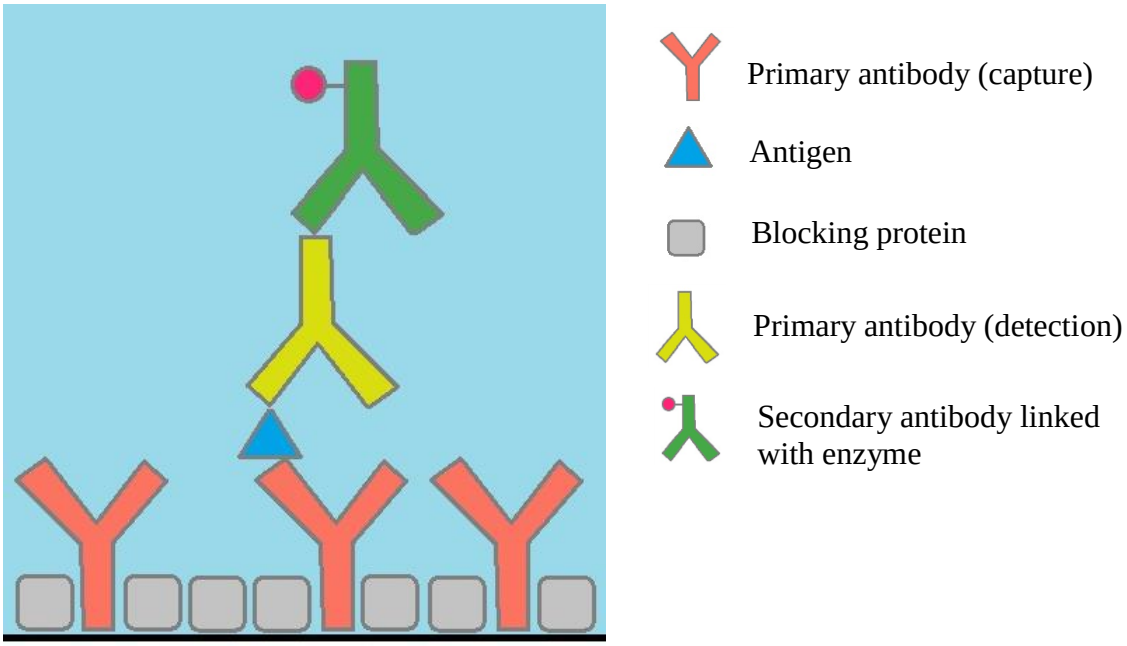

Figure 2-5: A schematic illustration of the sandwich assay ELISA method.

2.2.2 SPR Biosensing with Nanohole Arrays and Label-free Immunoassays

Development of optical sensors based on SPR for detection of chemical and biological analytes has drawn significant attention in the past decades[42]. SPR affinity immunoassays are the most effective label-free detection method used in biomedical analysis[48]. A transmission-based SPR biosensor (EOT grating coupling with nanohole arrays) was used in our group. The biosensor was integrated in microfluidic systems and the transmission setup, based on EOT, which has several advantages over the current technologies for low concentration detection of analytes[49].

For a SPR biosensor, the refractive index on the gold-dielectric interface changes when proteins adsorb to the surface due to the dielectric condition changes, as discussed in section 2.1.2. As shown in Figure 2-6, for the transmission SPR biosensor, when an antigen in solution binds to its specific antibody being immobilized on a gold surface with nanohole arrays, the interaction between the antigen and antibody leads to changes

in refractive index, resulting in a resonance wavelength shift of the enhanced transmitted light. The analyte of interest can be detected by monitoring the spectral shift.

Comparing to the standard immunoassay methods, such as ELISA, the transmission SPR detection is label free, rapid and low cost. Comparing to the common SPR biosensor with prism coupling, the transmission setup provides the possibility of lower detection limit, due to the small size of nanohole arrays; it is more amenable for miniaturization and overall device integration with the supporting optics[49]. The nanohole arrays can be fabricated with high reproducibility; and the geometric parameters of the nanohole structures can be optimized to improve sensitivity and detection limit of the device[49]. All of the above makes SPR biosensing with nanohole arrays a good candidate for future biomedical applications.

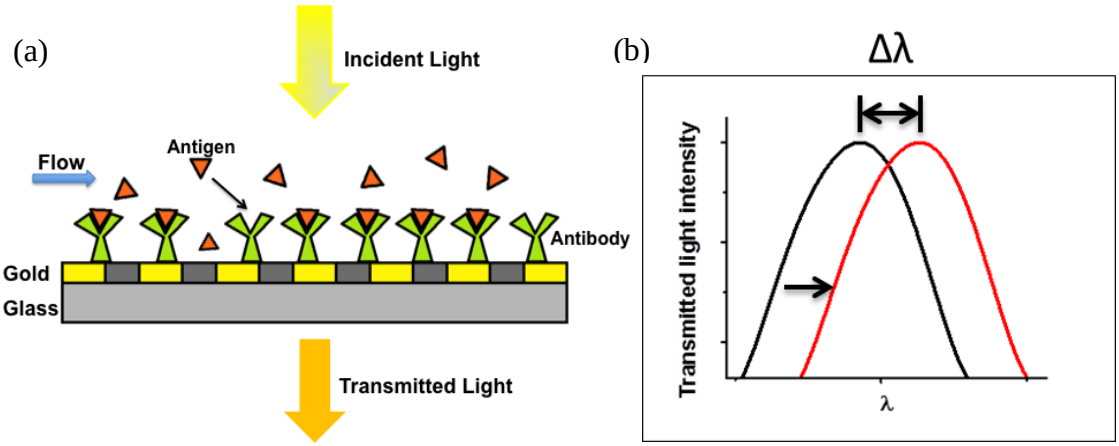

Figure 2-6: (a) Schematic illustration of an SPR biosensing experiment using nanohole arrays based on EOT. (b) Transmitted light spectrum shift due to the protein absorption to the gold surface.

2.2.3 Surface Binding Kinetics and Saturation for SPR Biosensing with Label-free Immunoassay

The kinetics of binding between antibodies and antigens at the liquid-solid interface for SPR biosensing has been widely studied[50]. Although we did not perform any kinetic experiment in this dissertation, a basic understanding of the kinetics of the immunoassay for SPR sensing will be helpful for the understanding of some of the results in our research. We can use a binding equilibrium situation to explain the course of an antigen-antibody binding for SPR biosensing with nanohole arrays, as shown below:

$$\mathbf{A(Antigen) + B(Antibody) \rightleftharpoons AB} \qquad \textbf{(2-9)}$$

In equation 2-9, A represents the antigen in solution, and B represents the antibody immobilized on the sensor surface. As illustrated in Figure 2-7, when antigen is added and starts to bind to the antibody on the sensor surface, a signal (spectral shift for the SPR experiment), proportional to the concentration of the antigen binding to the immobilized antibody on the gold surface (AB), is plotted against time. The initial rate of binding (or the change of the spectral shift) is proportional to the concentration of the antigen in solution[51] . As the number of antigens attached to the sensor surface increases and exceeds the antibody binding site capacity on the gold surface for a given solution concentration, the surface becomes saturated and the plot reaches a plateau. The amount of spectral shift at the plateau is then directly related to the concentration of the antigen in solution. However, at higher concentrations (assuming a Langmuir adsorption model in which multilayers are not formed), the surface reaches saturation and the position of the plateau will cease to respond to the surface concentration. In order to make a proper

quantification, we need to make sure that the concentration of the antibody immobilized on the gold surface is in the plateau region and that the solution concentration is far from allowing surface saturation.

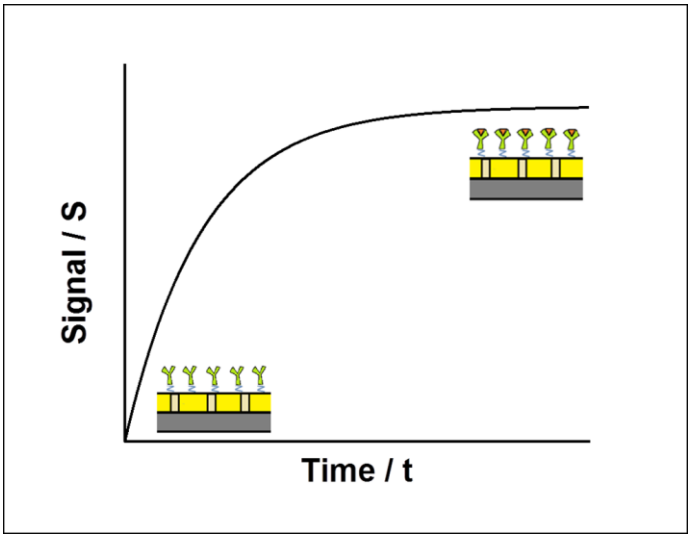

Figure 2-7: Schematic diagram of an affinity kinetic plot of antigen binding to antibody being immobilized on gold surface.

2.3 Biomarkers

In this thesis, the targets used for label free immunoassay detection by nanohole SPR are biomarkers that are overexpressed in cancer cells, as mentioned in section 1.1.6. We chose EGFR and CD19/CD20, which are overexpressed on the cell surface for lung cancer and leukemia, respectively[53,55]. By capturing these biomarkers using their specific antibodies immobilized on the gold sensor surface, the transmitted light spectra were monitored using the transmission SPR setup.

2.3.1 Epidermal Growth Factor Receptor (EGFR)

EGFR is a transmembrane protein and cell-surface receptor for the EGF extracellular protein ligands. Activation through ligand binding between EGF and EGFR triggers the protein-tyrosine kinase, leading to phosphorylation of key tyrosine residues for signal communication. EGFR plays an important role within a cell by regulating cellular activities, such as cell division[52]. Studies have showed that EGFR overexpression is frequently found in early-stage non-small cell lung cancers (NSCLC), making it an attractive biomarker target for the development of cancer diagnosis and anti-cancer therapeutic agent[53,54].

2.3.2 CD19 and CD20

Clusters of differentiations (CDs) are membrane proteins on lymphocytes (a type of white blood cell) of the immune system. They are functional cell surface proteins or receptors that can be measured from blood or other bodily fluids and biopsied samples. Over 250 CDs have been characterized, and they are classified by a CD number based on the type of monoclonal antibodies that are shown to bind to them. In normal individuals, the level of these molecules in blood is very low. However when the immune system is activated, the concentration of these molecules usually rises, which makes them perfect biomarkers for the diagnosis of diseases, such as leukemia, and AIDS[55]. We have chosen to develop a method for the detection of two CD biomarkers known as CD19 and CD20.

CD19 is an immunoglobulin (Ig) superfamily protein expressed on the surface of B lymphocytes. It is an important signal transduction molecule associated with other cell surface molecules on B cells. It is mostly found in the early stages of B cell development,

until plasma cell differentiation[56]. CD20 is also a protein expressed on the surface of B lymphocytes. It is involved in the regulation and proliferation of B cells, and acts as a cell surface complex regulating calcium transport across the plasma membrane. The protein exists on most of the stages of B cell development upon the differentiation into plasma cells[57]. Overexpression and fluctuation of the CD19 and CD 20 levels are associated with chronic lymphocytic leukemia (CLL)[58], which makes them perfect candidates as biomarkers for leukemia cancer diagnosis and treatment.

Chapter Three : Fabrication

Two types of nanohole array samples, fabricated using different techniques, were recorded on gold films for this dissertation. The two fabrication methods used were focused ion beam (FIB) milling and interference lithography (IL). The samples fabricated by FIB are identified in the dissertation as AuFIB, while AuIL were those made by IL. Details on the fabrication methods of these two types of samples will be discussed in this chapter.

3.1 Nanohole Arrays Fabricated by FIB

3.1.1 Nanohole Fabrication using FIB

AuFIB samples were fabricated using a Hitachi FB-2100 focused ion beam (FIB) system. The nanohole arrays were milled by FIB on commercial 100 nm-thick gold film deposited on a glass slide (Evaporated Metal Films)[59]. A 5 nm layer of Cr was applied to increase the adhesion between the gold and the glass. The gold-coated glass slide was first loaded into the vacuum chamber of the Hitachi system, and the beam was aligned and focused at the sample. A pattern of nanohole arrays was previously designed by software, with the desired hole shape, periodicity and size. The pattern was then be fabricated by the FIB using a gallium ion beam with energy of 10 keV. The resolution of 6 nm or better can be reached with this system[60]. All samples were fabricated using the equipment from the Advanced Microscopy Facility at the University of Victoria. The first two samples were fabricated by Mohammad Rahman, a visiting scientist from the Brolo group; the rest of the samples were fabricated by me.

3.1.2 Array Design

AuFIB samples contain four rows of five arrays each. Figure 3-1 demonstrates the footprint and the distance between the arrays. Each individual nanohole array was ~ 15 µm x 15 µm, and the distance between arrays was 200 µm and 275 µm from side to side, as indicated in Fig. 3-1. The periodicity of each array was 450 nm, and the diameter of each nanohole was 200 nm, as shown in Figure 3-2. Twenty arrays were fabricated on each sample, and distributed in multiple rows to allow the recording of multiple binding experiments at the same time.

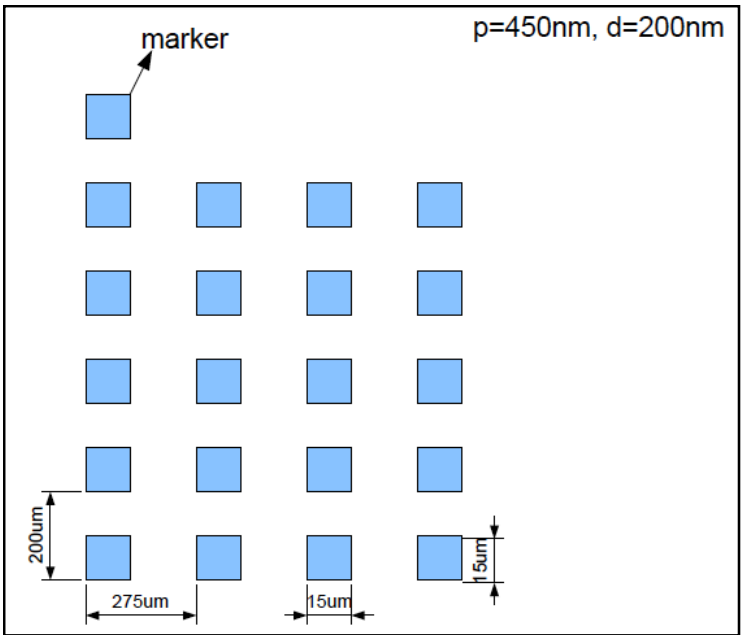

Figure 3-1: The design of the sample with 20 nanohole arrays with periodicity = 450nm, diameter = 200nm

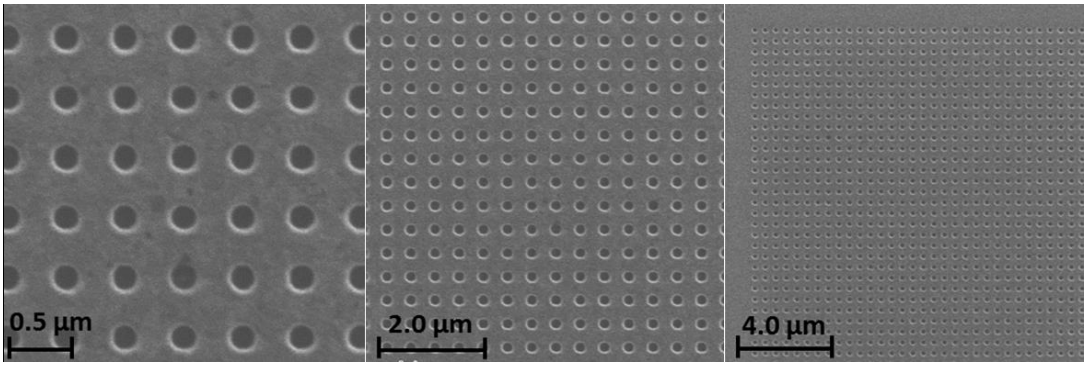

Figure 3-2: SEM images of a nanohole array at different magnifications with periodicity = 450nm, diameter = 200nm.

3.2 Microfluidic Fabrication

Microfluidic systems have found many applications in biochemical analysis and cell-based assays[61,62]. The nanohole arrays are just sensing elements, which require the support of a system to deliver molecules from solution to the sensor surface. Microfluidic channels made in soft polymers, in particular poly(dimethylsiloxane) (PDMS), are well suited for this type of application, with many advantages in terms of portability, cost, efficiency and automation[63]. In our experiments, a PDMS microfluidic chip was fabricated by soft lithography using a silicon master as a template for pattern replication. This technique enables rapid prototyping of microfluidic devices[64]. The microfluidic channels were designed using a CAD (computer-aided design) program.

3.2.1 Photolithography of the Silicon Master

The master for the PDMS microfluidic devices was fabricated by photolithography on a silicon wafer. The procedure of microfluidic fabrication is

illustrated in Figure 3-3. A layer of negative photoresist (SU-8 50) was spin coated to a silicon wafer at a spin rate of 1800 rpm for 30 seconds, generating a smooth layer of 100 μm as shown in Figure 3-3(a). The coated wafer was then prebaked at 65 ℃ for 10 minutes and then baked at 95 ℃ for 30 minutes. After baking, a high resolution pattern of the channels (designed using a CAD program, as will be discussed in section 3.2.3), printed on a transparency film (3M), was placed as a mask onto the photoresist layer (Figure 3-3(b)), and the system was exposed to UV light (~ 350 to 400 nm) for 100 seconds. During the exposure step, the negative photoresist exposed to the UV light was polymerized. After exposure, the wafer was post-baked at 65 ℃ for 1 minute and then baked at 95 ℃ for 10 minutes. A SU-8 developer was then applied to the wafer for 10 minutes to dissolve any unpolymerized photoresist, leaving a channel structure on the wafer, as can be seen from Figure 3-3(d). At last, the wafer (silicon master) was ready to be used for PDMS microfluidic chip replications.

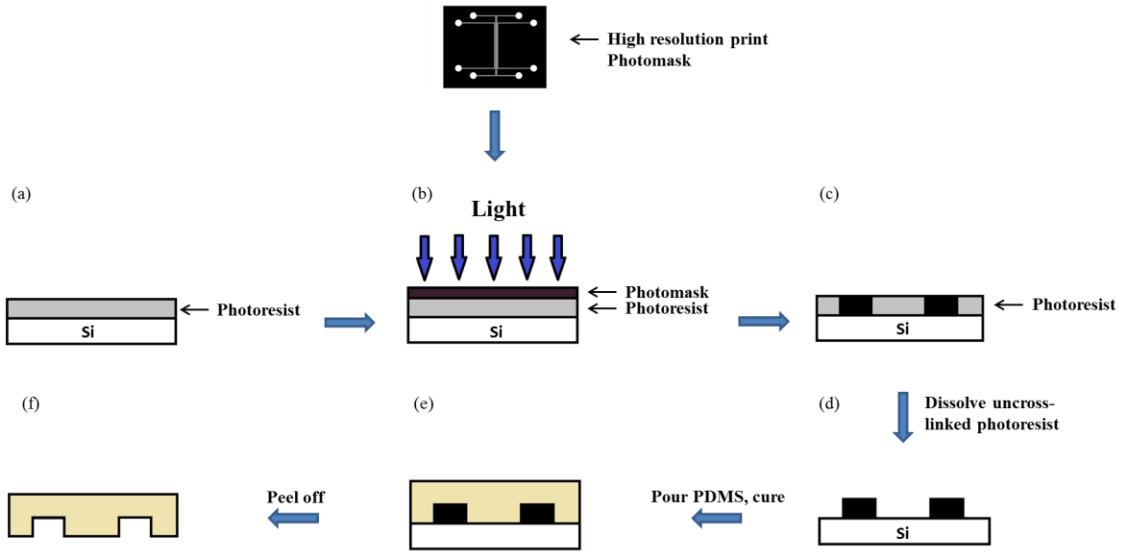

Figure 3-3: Schematic of the procedure for making silicon masters and PDMS microfluidic chip. (a) A silicon wafer is spin-coated with a photoresist. (b)A photomask is placed on top of the photoresist and the system is exposed to UV light. (c) Crosslinking occurs at the exposed photoresist. (d) The non-polymerized photoresist is dissolved by the developer. (e) PDMS prepolymer is poured on the silicon master and cured at ~ 80 ℃. (f) The PDMS microfluidic chip is peeled off the master. The regenerated master can be used for replication of the next PDMS microfluidic chip.

3.2.2 PDMS Microfluidic Chip

The PDMS chip with microfluidic channels was fabricated by mixing Sylgard 184 silicone elastomer base (~24g) and silicone elastomer (Dow Corning) curing agent (~2 g) in a 12:1 ratio by weight. The mixture was degassed under vacuum for 20 minutes to get rid of all gas bubbles. The mixture was then poured onto the silicon master, patterned with micro-channels, as described in section 3.2.3, and degassed again until no bubbles were found. After this, the master with a layer of PDMS on top (Figure 3-3(e)) was baked in an oven at 80 ℃ for 30 minutes. After baking, the cured PDMS was peeled off from the master. The channel inlets and outlets were punched on the PDMS mask using a hole

puncher (sensipress+, NWSL). The silicon master was recovered and used for the next PDMS chip replication.

3.2.3 Designing of the Microchannels

The microfluidic channels were designed using AutoCAD (Autodesk Inc., California), software that can generate high resolution graphic designs for print or machining operations[65]. As can be seen from Figure 3-4, the designed pattern for our experiments contains four channels parallel to each other. Each channel is about 100 μm in both width and height. After peeling the PDMS chip off from the silicon master, the middle region (iii) of the channels was aligned with the nanohole arrays of the AuFIB sample (pattern defined in Figure 3.1), with the channels right on top of the arrays, allowing solutions to flow over. As shown in Figure 3-4, the inlet channels (i) were used to flow a solution in, and the outlet channels (ii) collect the waste solutions.

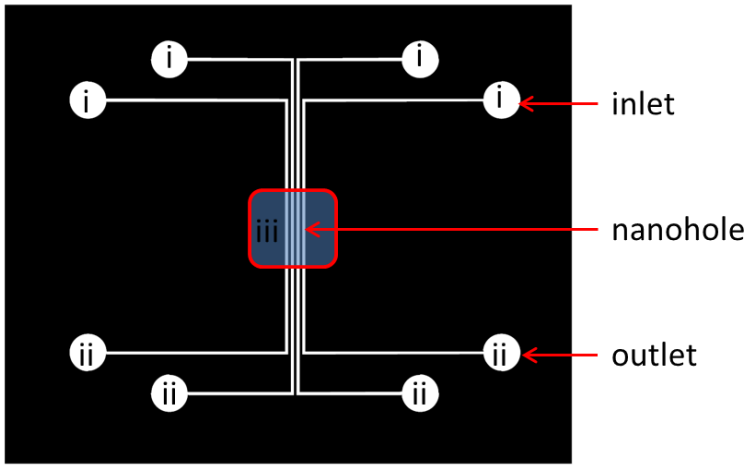

Figure 3-4: Microfluidic pattern designed by CAD. The channels are about 100 μm in width and height.

3.2.4 Array Alignment

The PDMS chip was aligned with the nanohole arrays of the AuFIB samples manually under an optical microscope. An actual picture of Region (iii) from Figure 3-4 was taken under the microscope, and it is shown in Figure 3-5. With the multiple channels, different experiments could be conducted at the same time. For example, the most left channel was used to flow the unknown sample, while the other channels were used for blank and control samples.

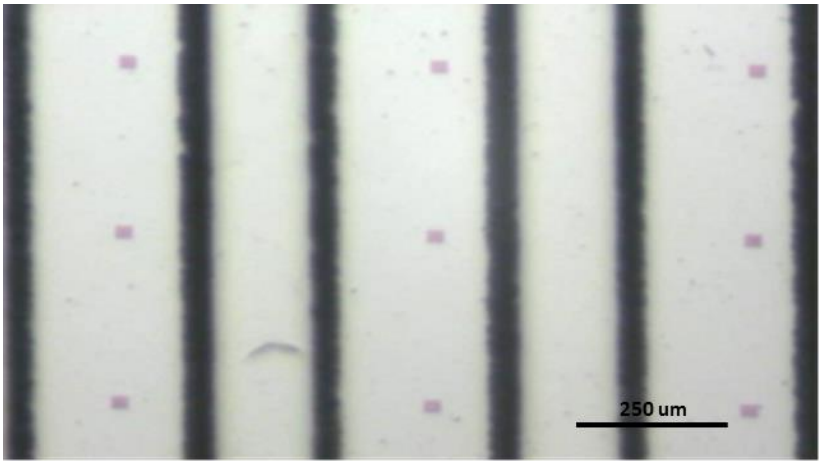

Figure 3-5: Optical Image of nanohole arrays from AuFIB Sample aligned with the PDMS microfluidic channels.

3.3 Large Area Nanohole Array Fabrication by Interference Lithography

3.3.1 Fabrication of Large Area Nanohole Array using Interference Lithography

Another method, interference lithography, was used to fabricate nanohole arrays with larger area. As demonstrated in Figure 3-6, a cleaned glass substrate was first spin-coated with 100 nm of SU-8 photoresist. The SU-8 photoresist layer was then exposed twice to the same interference fringe pattern rotating the sample $90\,^{\circ}$ between the exposures[66]. The fringe pattern generated by the interference of two plane waves was determined by the fringe period, which depends on the laser wavelength and the angle formed between the interfering beams[66]. The fringe pattern was generated by 458 nm Melles Griot solid-state laser[67]. A square array of photoresist columns was formed as shown in Figure 3-6(b) after being developed in Microposit 351 Developer (Rohm and Haas). The photoresist columns were coated with 100 nm Au film by thermal evaporation. At last, a lift-off step removed the photoresist columns leaving the substrate patterned with a nanohole array, as it can be seen from Figure 3-6(d). The size of the patterned area region resulted from IL can be ~2 x 2 cm^2. The size and periodicity of the nanoholes depends on the fringe period, exposure dose and development time[66]. All samples were fabricated by Jacson Menezes (a Postdoctoral Fellow from the Brolo group) using the equipment from the Diffractive Optics Lab at Universidade Estadual de Campinas (www.unicamp.br).

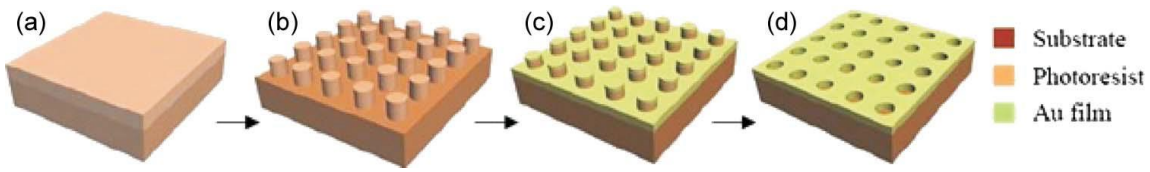

Figure 3-6: Scheme of nanohole fabrication using IL. (a) Photoresist spin coated onto the glass. (b) Double Exposure of two-beam interference pattern followed by photoresist development. (c) Au film deposition by thermal evaporation. (d) Life-off of the photoresist. "With kind permission from IEEE Photonics Journal: < Comparison of Plasmonic Arrays of Holes Recorded by Interference Lithography and Focused Ion Beam, 4, 2012, 544, Menezes, J., Barea, L., et al., figure 2>."

3.3.2 Array Design

AuIL samples was fabricated by IL and used in the whole cell capture experiments reported in this thesis in Chapter Six. Compared to the AuFIB samples, with array size of ~ 15 x 15 μm^2, AuIL samples have a much larger area patterned with nanoholes, ~ 2 x 2 cm^2 (Figure 3-7). The large area simplifies alignment and it is more suitable for whole cell detection coupled with SPR[68]. As shown in Figure 3-8, the periodicity of the array was 500 nm, and the diameter of each nanohole was 200 nm. A layer of SU-8 photoresist was used to increase the adhesion between the Au layer and the glass slide[69]; however the sample was still too delicate to be repeatedly used (further discussed in section 4.2.2), and each sample was used for only one experiment. Due to the delicateness of the sample, all experiments done with AuIL samples were recorded in air instead of being assembled with the PDMS chip.

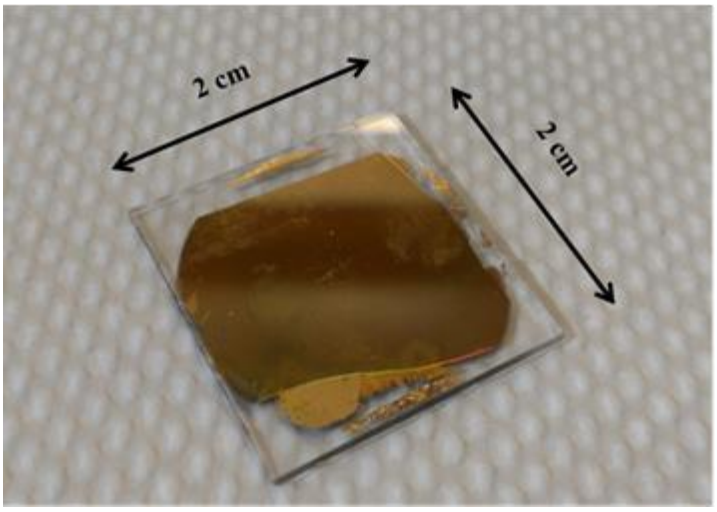

Figure 3-7: Picture of AuIL Sample fabricated by IL with nanohole area of 2 x 2 cm^2.

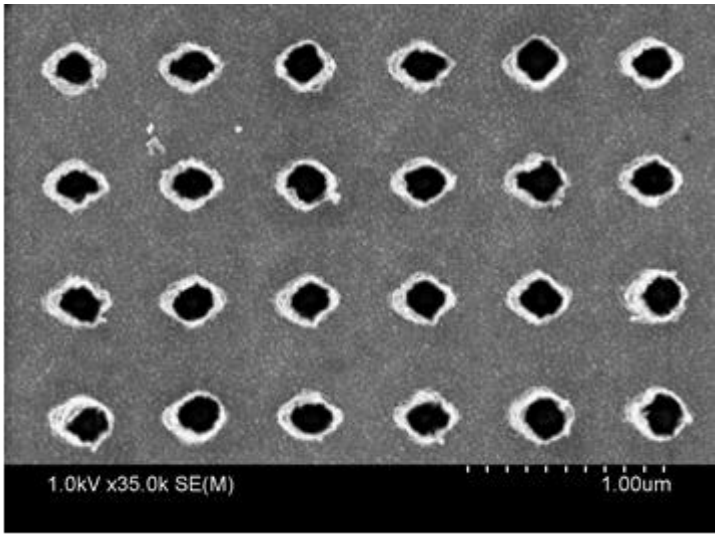

Figure 3-8: SEM image of AuIL Sample fabricated by IL (periodicity = 500nm, diameter = 200nm)

Chapter Four : Experimental

4.1 Detection of EGFR and CD19/20 Biomarkers Experiment

4.1.1 Materials

4.1.1.1 EGFR Antibody and Antigen

The EGFR peptide (antigen) and antibody were purchased from Abcam, Cambridge, USA (No. Ab2432 and Ab2430). The EGFR peptide is a synthetic peptide (a fragment of the EGFR antigen) containing one protein kinase domain. The EGFR antibody is rabbit polyclonal to EGFR corresponding to C terminal amino acids 1005-1016 of EGFR. The original EGFR peptide and antibody concentrations provided are 0.1 mg/mL and 0.2 mg/mL, respectively. For a particular experiment, the original EGFR peptide and antibody were diluted using PBS buffer solution to the desired concentration. The EGFR peptide and antibody solutions were stored at -20 ℃ before used.

4.1.1.2 CD19 and CD20 Antibodies

The CD19 and CD20 antibodies were purchased from eBioscience, California, USA (No. 14-0199 and 14-0209). They are both monoclonal antibodies that react with human CD19 and human CD20 transmembrane proteins, respectively. The original concentrations of CD 19 and CD20 antibodies were both 0.5 mg/mL. For a particular experiment, the original CD 19 and CD20 antibodies were diluted with PBS buffer solution to the desired concentration. The antibody solutions were stored at -20 ℃ prior to use.

4.1.1.3 Cell Lines

The A549 cell line was purchased from ATCC, Manassas, USA (No. CCL-185). The H520 cell line was provided by Rob Sahota from the BCCA-Vancouver Island Centre. The A549 cell line was initiated in 1972 through explant culture of lung carcinomatous tissue from a 58-year-old Caucasian male, and it is EGFR positive. The cell is grown in F-12K medium with 10% fetal bovine serum at 37 ℃. The H520 cell line is EGFR negative and was derived from a sample of lung tissue taken from a patient with squamous cell carcinoma in 1982. The cell is grown in RPMI-1640 medium with 10% fetal bovine serum at 37 ℃. Both cell lines were lysed with NP40 lysis buffer solution for the biomarker detection experiment, and their concentrations were validated by ELISA.

The CRL 3000 and CCL 155 cell lines were also purchased from ATCC, Manassas, USA (No. CRL-3000 and CCL-155). The CRL 3000 cell line was derived from a sample of peripheral blood taken from a 64 years-old Caucasian man with mantle cell lymphoma, and it is CD19 and CD20 positive. The cell is grown in RPMI-1640 medium with 15% fetal bovine serum at 37 ℃. The CCL 155 cell line was cultured from peripheral blood collected from a 61-year-old male with plasmacytoma, and it is CD19 and CD20 negative. The cell is grown in RPMI-1640 medium with 10% fetal bovine serum at 37 ℃. Both cell lines were lysed with NP40 lysis buffer solution for the SPR biomarker detection experiment and ELISA.

4.1.1.4 Lysis Buffer

NP40 (Nonidet-P40) buffer was provided by Rob Sahota from the BCCA-Vancouver Island Centre. It contains 150mM NaCl, 0.1% Triton X-100, 50mM Tris-HCl

(pH 8.0) and protease inhibitors[70]. NP40 is a non-ionic detergent to solubilize proteins in a biologically active form[70], which was used for the extraction of EGFR, CD19 and CD20 from cells for our SPR biomarker detection experiment. The buffer was stored at 4 ℃ prior to use.

4.1.1.5 Chemicals

Unless otherwise noted, ACS reagent grade chemicals were used for this research project. N-hydroxysuccinimide (NHS), 1-ethyl-3-(3-dimethylaminopropyl)carbodiimide (EDC), phosphate buffered saline (PBS) and bovine serum albumin (BSA) were purchased from Aldrich Sigma, St. Louis, MO. The carboxyl PEG-thiol compound with molecular weight of 3000 Dalton (α-mercapto-ω-carboxy poly(ethylene glycol)) was purchased from RAPP Polymere GmbH, Tuebingen, Germany. All water used was obtained from a Barnstead NANOpure Diamond water purification system with a resistivity greater than 18.2 MΩ·cm.

4.1.2 Cell Lysate Procedure

The biomarkers of interest were detected from cell lysates. Different cells lines were lysed to release their surface proteins using lysis buffer solutions. This solubilizes the proteins allowing them to travel in a microfluidic channel integrated with our nanohole arrays biosensors[70]. Lysis buffers differ in their ability to solubilize proteins. Those containing higher concentrations of detergent provide higher yield, but are harsher than the others[71]. If the antibody recognizes a linear peptide of the protein, a harsh

denaturing lysis buffer can be used. However, if the antibody is directed toward a conformational peptide in the wild protein, a gentler lysis buffer should be used (e.g., NP40) [71]. In this dissertation, the biomarkers of interest were located on the cell membrane and a gentler NP40 lysis buffer was used.

Both the A549 and H520 cells were grown as monolayer cultures and were lysed the same way in order to release EGFR biomarkers from the cell surface. The cells were washed twice with ice-cold PBS after the culture medium being discarded. Then 1.0 mL NP40 lysis buffer was added into the culture dish, and the cells were rapidly scraped with a cell scraper to remove and lyse residue cells. Then the cell lysate were transferred to a microcentrifuge tube and incubated on ice for 30 minutes with vortexing occasionally. The lysate was centrifuged at 20,000 x *g* for 20 minutes at 4℃. The supernatant was carefully removed to a fresh tube, and stored at -80℃ before used for the SPR detection and ELISA. The cell pellet was discarded.

The CRL3000 and CCL155 cells were lysed using a similar procedure as descried above. However these two cell lines were grown as suspension cultured cells; therefore, instead of scraping from the dish, the suspended cells were first transferred to a 15mL centrifuge tube and pelleted by centrifuging at 450 x *g* for 5 minutes. The medium was removed by aspiration. Then 5.0 mL ice-cold PBS was added to the tube. After mixing briefly to re-suspend the cells, they were centrifuged for 5 minutes at 450 x *g* and the supernatant was removed. This washing step was repeated 2 times, and then 1.0 mL of NP40 lysis buffer was added to the washed cell pellet and mixed briefly. After incubating on ice for 30 minutes with occasional vortexing, the cell lysate was centrifuged at 20,000

x *g* for 20 minutes at 4 ℃. The supernatant were carefully removed to a fresh tube, and stored at -80 ℃ for future use. The cell pellets were discarded.

4.1.3 ELISA Procedure

A sandwich ELISA, as described in section 2.2.1, was used to determine the EGFR concentration in the A549 and H520 cell lysates. A complete ELISA kit for human EGFR detection was purchased from Invitrogen, New York, USA (No. KHR9061). It contains all the required solutions, antibodies, and standards; a polystyrene plate with 12 x 8 well strips was also included which has been pre-coated with EGFR capture antibodies. After bringing the pre-coated plate to room temperature, 100 µl of the A549 and H520 cell lysates (diluted 50 times with PBS) and the human EGFR standards with concentration ranged from 0 to 20 ng/mL (0, 0.312, 0.625, 1.25, 2.5, 5, 10, 20 ng/mL prepared by a serial dilution) were added to each well for 2 hours at room temperature. The plate was washed 4 times with the wash buffer solution, and 100 µL of the human EGFR detection antibody was added to each well for 1 hour at room temperature. After the incubation period, the plate was washed, and 100 µL of the HRP-conjugated anti-rabbit IgG (secondary antibody) was added to each well for 30 minutes at room temperature. Then the stabilized chromogenic, TMB was added (100 µl per well) followed by incubation in the dark at room temperature for 30 minutes. At last 100 µl of the stop solution was added to each well, and the solution in the wells turned from blue to yellow. The absorbance of each well was read at 450 nm, and a calibration curve was generated to determine the amount of EGFR from the cell lysates. The results from an ELISA test to the presence of EGFR are shown in Figure 4-1.

Figure 4-1: An ELISA to test for EGFR in A549 and H520 cell lysates.

Two complete ELISA kits for CD19 and CD20 detections were purchased from Antibodies-online Inc., Georgia, USA (No. ABIN417761 and ABIN417586). Similar to the procedure described above, a sandwich assay ELISA was used to determine the CD19 and CD20 concentrations in the CRL 3000 and CLL 155 cell lysates. For the CD19 ELISA kit, 100 µl standards with concentration ranged from 0 to 20 ng/mL (0, 0.312, 0.625, 1.25, 2.5, 5, 10, 20 ng/mL prepared by a serial dilution) were added to each well that were pre-coated with the CD19 capture antibody. The CRL 3000 and CLL 155 cell lysates were diluted 100 times with PBS before tested by ELISA. For the CD20 ELISA kit, both cell lysates were diluted 200 times with PBS, and the CD 20 standards were prepared by a serial dilution with concentration ranged from 0 to 80 ng/mL (0, 1.25, 2.5, 5, 10, 20, 40, 80 ng/mL). The absorbance of each well was measured at 450 nm.

4.1.4 Sample Surface Modification

In order to immobilize the antigen or antibody protein onto the gold surface efficiently, the gold sample needs to be pre-modified with carboxyl PEG-thiol polymer. The thiol group binds to the gold surface forming a self-assembled monolayer (SAMs)[72]. By briefly incubating the PEG-modified sample with EDC and NHS solution, the carboxyl end of the PEG monolayer converts into a semi-stable primary amine-reactive NHS ester, which later undergoes substitution reaction with the primary amine groups of the protein forming a stable amide bond[73], as shown in Figure 4-2.

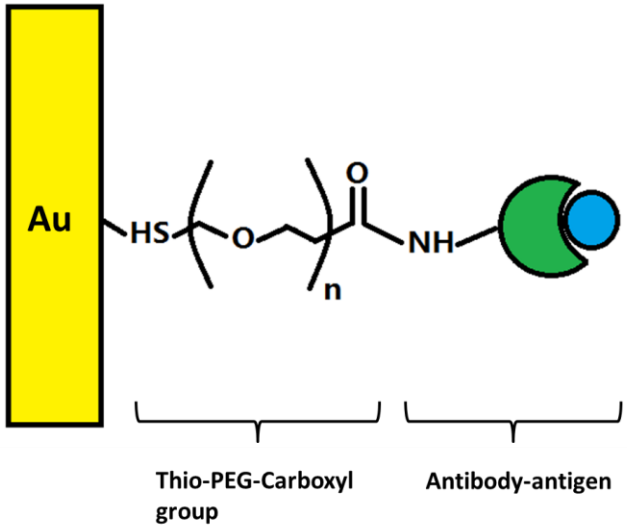

Figure 4-2: Schematic representation of the PEG monolayer binding with protein on gold surface

AuFIB samples were used for the detection of EGFR, CD19 and CD20 biomarkers in this dissertation. The samples were first modified with the carboxyl PEG-thiol polymer (200 μM) by incubation overnight. Then this sample was incubated with EDC (75 mM) and NHS (15 mM) solutions for 30 minutes in PBS. It was washed with

DI water and dried with N_2 after being immersed in the antigen or antibody solution (10 µg/mL) for two hours. A layer of the protein was then formed on the gold surface.

4.1.5 SPR Experiment Setup

Figure 4-3(a) shows the SPR transmission experimental setup of the optical measurements for both the EGFR and CD19/20 biomarker detections. A broadband white light source from a 50 watt halogen lamp was provided. The light was focused on the gold sample using a 50x long working distance microscope objective (Olympus, Japan). The light that passed through the nanohole arrays on the gold sample was then collected by an optic fibre connected to a spectrometer. The transmission spectra were recorded and analyzed by the data acquisition software (Ocean Optics – OOIBase 32 Platinum). As shown in Figure 4-3(b), the sensor device was assembled with two aluminum plate holders with screws. It consists of three main layers. The top layer was an acrylic plate used to stabilize the other two layers. The middle was the microfluidic layer (made of PDMS) with 275 µm width channels, allowing solutions to flow on top of the sensing area (section 3.2.3). The bottom layer was a glass slide sample coated with a gold film where the nanohole arrays were located (section 3.1.2).

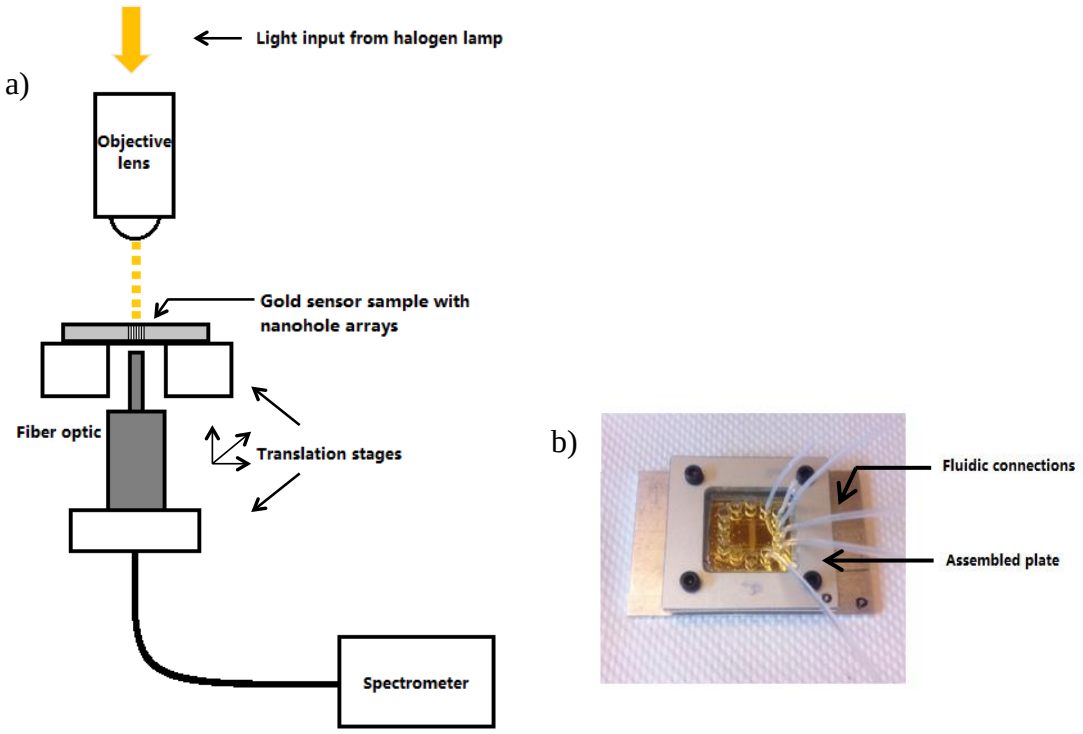

Figure 4-3: (a) Schematic setup for the transmission measurements through nanohole arrays of gold sensor sample. (b) The assembled gold sensor sample device with fluidic connections.

4.1.6 Spectrum Measurement

As described in section 2.2.2, the transmitted light spectrum of the arrays will show a red-shift in the wavelength if the dielectric properties of the surface changes due to molecular adsorptions[49]. This process is illustrated in Figure 2-6. When a molecule (i.e. antigen or antibody) is absorbed onto the arrays, the interface refractive index will change, leading to a red-shift in the transmission spectrum. All spectra are normalized against their maximum transmission intensity to 1. By measuring the shift in the wavelength at 95% normalization, the adsorption of the molecule (i.e. antigen or antibody) is quantified.

4.1.7 Sample Cleaning

In order to recover the surface after the protein modification, the AuFIB samples were cleaned between each experiment by sonication in acetone for 5 minutes, in ethanol twice for 10 minutes each and in methanol twice for 10 minutes each. The sample was then placed in the plasma cleaner (Harrick) under vacuums at high RF level for 5 to 10 minutes. After the cleaning procedure, transmission spectrum of the sample was checked to make sure that the EOT peak was back to its original wavelength, indicating that the sample was clean. The sample was also checked by Fourier transform infrared spectroscopy (FTIR) once every month for the cleanness of the gold surface.

4.2 Whole Cell Capture Experiment

4.2.1 Materials

4.2.1.1 EGFR Antibody

The EGFR antibody purchased from Abcam as mentioned in section 4.1.1.1 was used here for the whole cell capture experiment. The antibody was diluted with PBS to the desired concentration and stored at -20 ℃ before used.

4.2.1.2 A549 and H520 Cell Lines

A549 and H520 cell lines, the same ones for the EGFR biomarker detections as mentioned in section 4.1.1.3, were used here for the whole cell capture experiments. The

concentration of the cell suspension was determined by hemocytometer (Hausser Scientific, USA).

4.2.1.3 Samples for the Whole Cell Capture Experiments.

AuIL samples, fabricated by interference lithography, were chosen for the whole cell capture experiment. As shown in Figure 3-7, AuIL has a layer of 100 nm thick gold coated on a glass slide with a nanohole-structured area of ~ 2 x 2 cm^2 (diameter = 200 nm, periodicity = 500 nm). A detailed introduction of sample fabrication was described in Chapter three.

4.2.2 Sample Cleaning

Attempts to clean the AuIL samples before the experiment showed that the gold layer came off easily from the glass after more than 30 seconds of sonication in ethanol. This introduced difficulties in terms of recovering the surface for further experiments, since ethanol is required in the cleaning protocols of gold surface [74]. Due to the delicateness of the sample in terms of cleaning, each sample was sonicated for a shorter period of time and only used once for each experiment. The sample was cleaned before the experiment by sonication in acetone for 1 minute and in ethanol three times for 10 seconds each. It was then placed in the plasma cleaner (Harrick) under vacuum at high RF level for 5 minutes. At last, the sample was rinsed with DI water, ethanol and dried with a stream of N_2 before use.

4.2.3 Sample Surface Modification

A similar surface modification method as mentioned in section 4.1.4 was introduced here for the cell capture experiment. After cleaning, the surface of the AuIL sample was modified with thio-PEG polymer (200 μM) by incubation overnight. Then EDC (75mM) and NHS (15 mM) in PBS were added to the sample and incubated for 30 minutes. After being washed with DI water and dried by a stream of N_2, the sample was immersed in EGFR antibody solution (10 μg/mL) for two hours. A layer of EGFR antibody was formed on the gold surface. Instead of using a PDMS microfluidic chip to flow the cell suspension, the pre-modified AuIL sample was placed in a six-well plate, where 1 ml of the cancer cell suspension was seeded to the sample at a concentration of 4.8×10^4 cells/mL. The plate was placed in an incubator (Thermo Scientific, USA) for cell cultures at 37 ℃ with 5% CO_2 in air atmosphere for 45 minutes, and washed three times with PBS to remove the unbound cells followed by drying with a stream of N_2. A layer of cells was formed on the gold surface and ready for the next step as demonstrated in Figure 4-4.

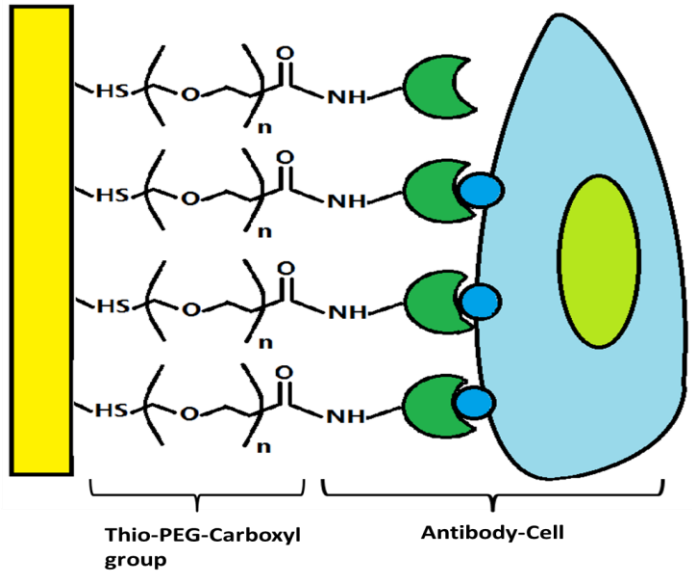

Figure 4-4: Schematic representation of the PEG monolayer binding with cells on gold surface.

4.2.4 Cell Detection with Microscopy Imaging

After the modifying step, AuIL samples with immobilized cells were then examined under a microscope (Leica, Germany) in air. The cancer cells being captured were counted within an area of 4 mm^2 at four different locations on the same sample. The average number of cells being captured was calculated and compared with the control samples.

4.2.5 SPR Spectrum Measurement

A transmission spectrum through the nanoholes was recorded in air for the AuIL sample (modified with EGFR antibody) before and after the cell capture at four different locations on the same sample. The spectral shift was determined using the same SPR transmission experiment setup explained in section 4.1.5. The average spectral shift

resulted from cell capture was calculated and compared between A549 and H520 cell lines.

Chapter Five : Detection of EGFR Lung Cancer and CD19/CD20 Leukaemia Cancer Biomarkers

In this dissertation, the detections of three different biomarkers from two different cancers are examined using the nanohole-based surface plasmon resonance (SPR) biosensing technique. The three biomarkers are EGFR, related to lung cancer; CD19 and CD20 from leukaemia cancer cells. Two surface modification methods were implemented for the EGFR detection. The concentrations of the three biomarkers in cell lysate solutions were also determined by ELISA. In this chapter, the detailed experimental data and results for both the nanohole SPR and ELISA detections will be discussed.

5.1 Introduction

5.1.1 Calibration using Glucose Solution

Glucose solutions of different concentrations were used to quantify the sensitivity of the AuFIB sample (described in Chapter three) to changes in bulk refractive indexes. Glucose solutions with concentrations ranging from 0.005M to 1.2M (refractive index ranging from 1.333 to 1.364) were flowed into the PDMS microfluidic channels on top of the nanohole arrays on gold. A transmission spectrum from each nanohole array was obtained for all glucose solutions (experimental setup described in section 4.1.5). The refractive index of each solution was measured by a commercial refractometer (pocket refractometer, ATAGO). By plotting the wavelength of the maximum transmission against the bulk refractive index for each glucose solution, the sensitivity of the AuFIB

samples, in nm/RIU (RIU = refractive index units), and resolution, in RIU, were obtained from the slope of the linear-fit plot and the standard deviation of the lowest concentration of glucose solution. A noise level of the spectral shift measurement was also obtained by monitoring the transmission spectral shifts for the 0.35M glucose solution over a period of 34 seconds.

5.1.2 EGFR Detection using Nanohole-SPR Transmission Experiment

Two detection schemes were employed for the EGFR experiments. In preliminary experiments, the EGFR peptide was immobilized on the gold surface, and a solution of the EGFR antibody was flowed through the PDMS channels to bind to the immobilized antigen. The first setup was conducted to test if the surface chemistry works since the EGFR antibody has a larger molecular weight (than the EGFR peptide)[75] and easier to be detected with a larger wavelength shift resulting from greater refractive index change[76]. In the other arrangement, the EGFR antibody was immobilized on the gold surface and the EGFR antigen was detected from the solutions. The second setup is more realistic for biomarker detections where EGFR antigen is the target of interest for cancer diagnosis[53,54].

5.1.2.1 Detection of EGFR Antibody

Figure 5-1 demonstrated the procedures for the EGFR antigen-antibody binding procedures with the microfluidic device. The channels were filled with PBS, and the transmission spectrum for each array was obtained. After that, the EGFR antibody solution in PBS was introduced to the EGFR antigen monolayer via the PDMS channels

for 45 minutes at a rate of 0.02 mL/min allowing the specific binding between the EGFR antigen and antibody. Then the channels were flushed with PBS again to remove any unbounded EGFR antibody, and the transmission spectrum of each array was obtained. The spectral shifts before and after the EGFR antibody binding (obtained in PBS) were measured.

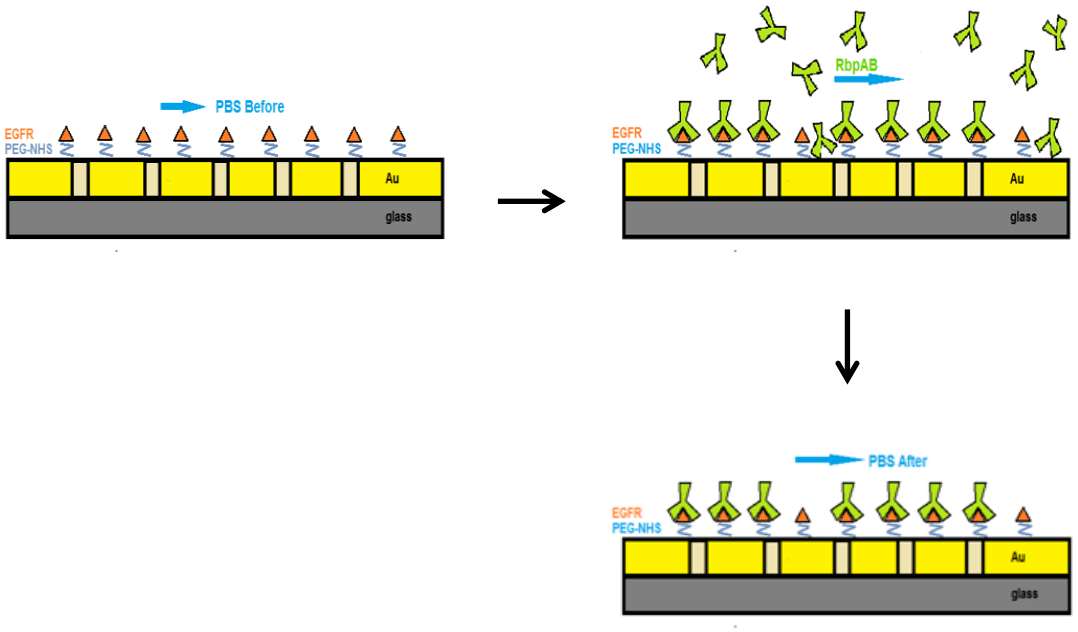

Figure 5-1: Schematic presentation of the EGFR antigen-antibody binding procedures.

5.1.2.2 Detection of EGFR Antigen

The procedure for the detection of EGFR antigen is the same as the procedure described in section 5.1.2.1. However the EGFR antibody solution (10 μg/mL) was immobilized on the gold surface and EGFR antigen in different solutions were flown over and detected by measuring the spectral shift before and after the binding. The procedure of the EGFR antibody-antigen binding system is shown in Figure 5-2.

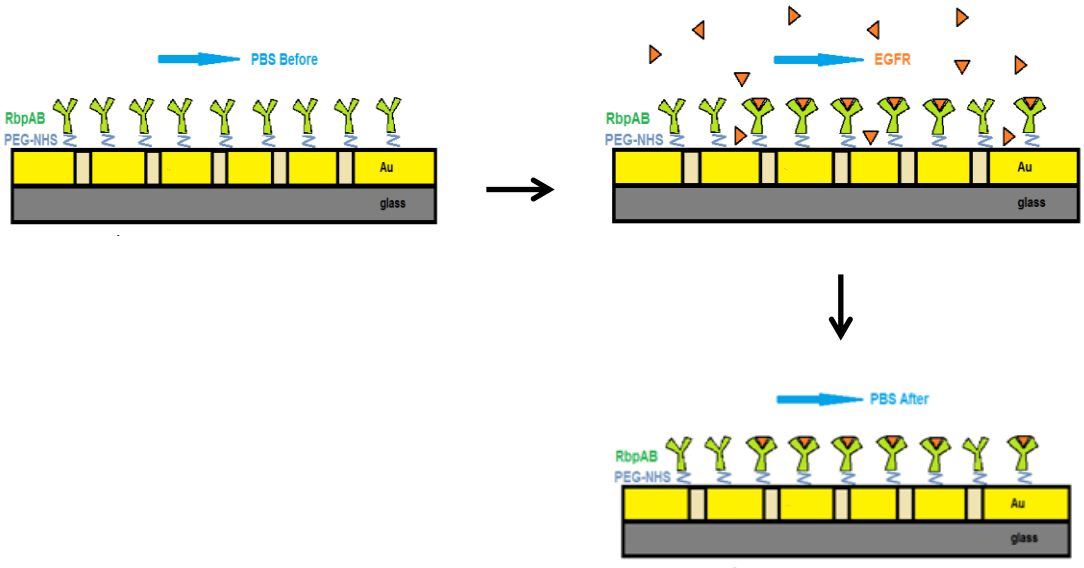

Figure 5-2: Schematic presentation of the EGFR antibody-antigen binding procedures.

5.1.3 CD19 and CD20 Detections Detection using Nanohole-SPR Transmission Experiment

Only one type of experimental setup was used for the detection of CD19 and CD20 antigens. Similar to the procedure mentioned in section 5.1.2.2. After the pre-modification of the AuFIB sample with CD19 or CD 20 antibody (10 µg/mL), cell lysate solutions containing CD19 or CD20 antigens were flowed over and detected by measuring the spectral shifts before and after the bindings.

5.2 Results and Discussion

5.2.1 Calibration using Glucose Solutions

Glucose solutions with different concentrations were used to calibrate the sensitivity of the nanohole arrays in the AuFIB sample by monitoring the shifts in transmission spectrum in respect to the change in bulk refractive indexes. As shown in Figure 5-3, a red shift was observed with an increased concentration (or refractive index) of the glucose solutions, which is consistent with the established theory of optical transmission through nanohole arrays[76] as described in Chapter two.

The spectral shift at maximum transmission was plotted against the solutions refractive index, as shown in Figure 5-4. The slope of the plot demonstrated a sensitivity of 554 ± 6 nm/RIU for the AuFIB sample (periodicity of 450 nm). Using the results from Figure 5-4, it is possible to calculate an important sensor performance parameter in SPR called resolution. Resolution is the minimum detectable variation in refractive index units (RIU) by the sensor platform. The sensor resolution was determined to be 6.8×10^{-5} RIU by dividing the standard deviation of $\Delta\lambda$ (of the lowest concentration glucose solution) by the sensitivity. The performance of our sensor is comparable to the current reported results from the nanohole array SPR experiment (470nm/RIU)[77] .

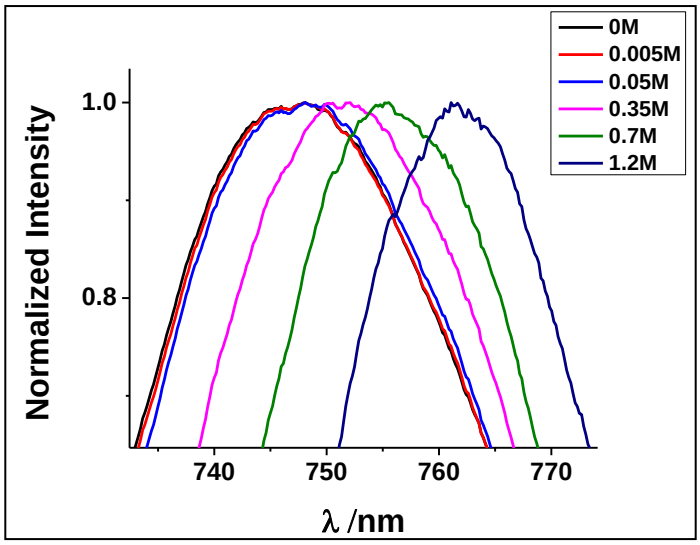

Figure 5-3: The transmission spectra of one nanohole array in response of increased concentration of glucose solutions. The periodicity of each array is 450 nm, and the diameter of the holes is 200 nm.

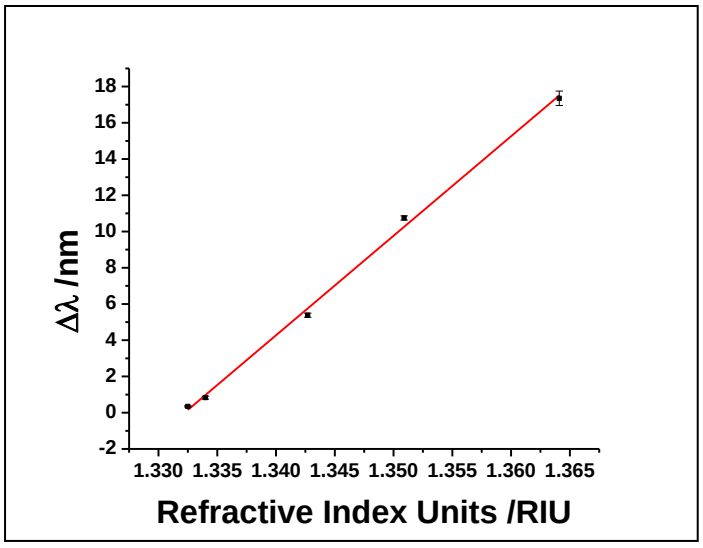

Figure 5-4: The spectral shift at maximum transmission for the AuFIB sample (periodicity = 450 nm, diameter = 200 nm) in contact with the four glucose solutions with different concentrations as a function of refractive index. The slope was 554 nm/RIU.

As shown in Figure 5-5, the noise level of the spectral shift was also measured by monitoring the wavelength shift of the glucose solution (0.35M) every 2 seconds with 2 spectra averaged for a total of 34 seconds. The standard deviation of the noise (σ) was determined to be 0.03 nm. The minimum shift that we could detected, commonly defined as a signal-to-noise ratio (S/N) of three, was determined to be 0.09 nm (3 x σ).

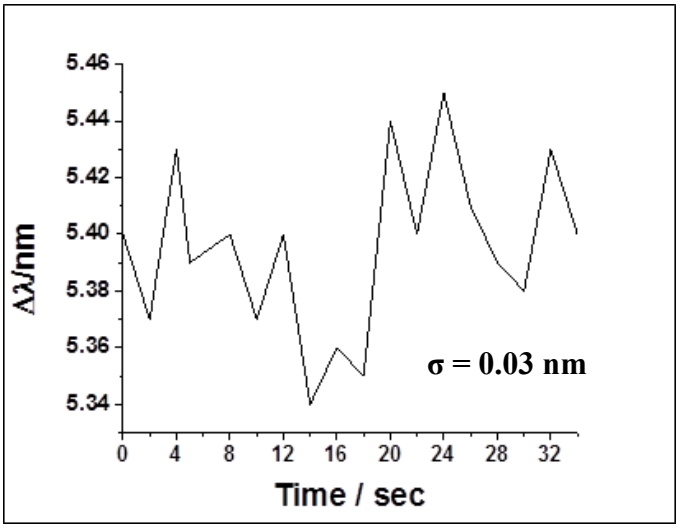

Figure 5-5: Noise level of the spectral shift at maximum transmission in contact with glucose solution (0.35M). With 2 sec temporal resolution, the noise for spectrum shift (σ) is 0.03 nm.

5.2.2 Detection of EGFR Antibody and Antigen

5.2.2.1 Detection of EGFR Antibody

The EGFR antigen (peptide) was first immobilized on the gold surface as described in section 4.1.4, and the EGFR antibody in PBS was detected. Figure 5-6(a) shows a typical spectral red-shift after the EGFR antibody binding to the immobilized antigen for one of the arrays. A consistent red-shift was observed for the four different

arrays with the same periodicity, as shown in Figure 5-6(b). The average wavelength shift ($\Delta\lambda$) was ~2.2 ± 0.2 nm, indicating an increased interface refractive index resulting from the EGFR antibody adsorption[78].

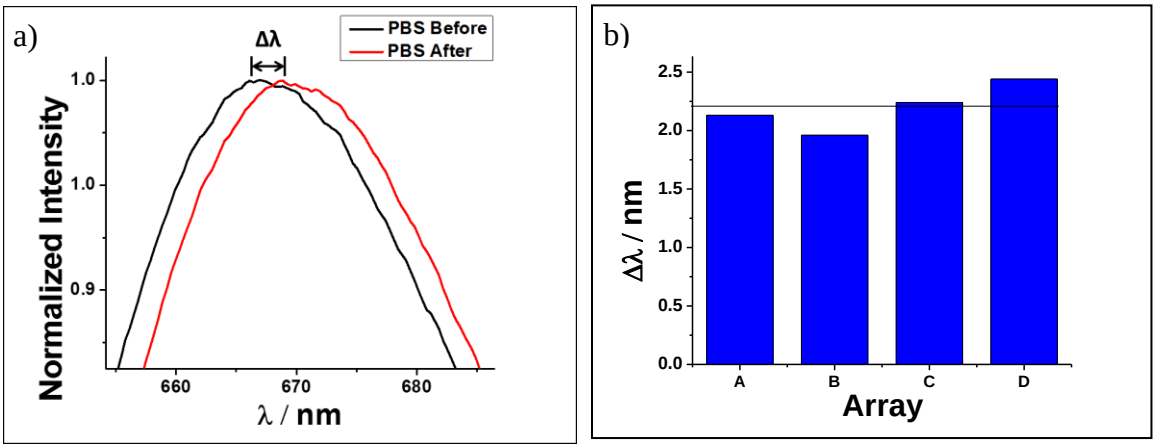

Figure 5-6: (a) Transmission spectra for one nanohole array before and after the EGFR antigen-antibody interaction [EGFR Antibody] = [EGFR peptide] = 10 μg/mL. (b) Wavelength shift of four nanohole arrays with the same periodicity (periodicity = 450 nm, diameter = 200 nm) before and after the EGFR antigen-antibody interaction.

EGFR antibody was then diluted with PBS to different concentrations, ranging from 0 to 15 μg/mL. The transmission spectrum of one array was measured as the EGFR antibody with different concentrations was flowed through the microfluidic channels after the antigen immobilization. As shown in Figure 5-7(a), an increased red-shift was observed as the concentration of the antibody increases, which suggested that more antibodies were absorbed to the surface with the increasing concentration. The spectral shifts were calculated using the spectrum of 0 μg/mL antibody solution as reference and plotted against concentration in Figure 5-7(b). As the concentration of the EGFR antibody increased from 1 to 15 μg/mL, the spectral shift increased from 1.1 to 1.9 nm,

respectively. A linear calibration curve was plotted, and the sensitivity of the antibody detection was determined to be 0.05 nm/μg·mL^{-1} from the slope of the calibration curve as shown in Figure 5-7(b).

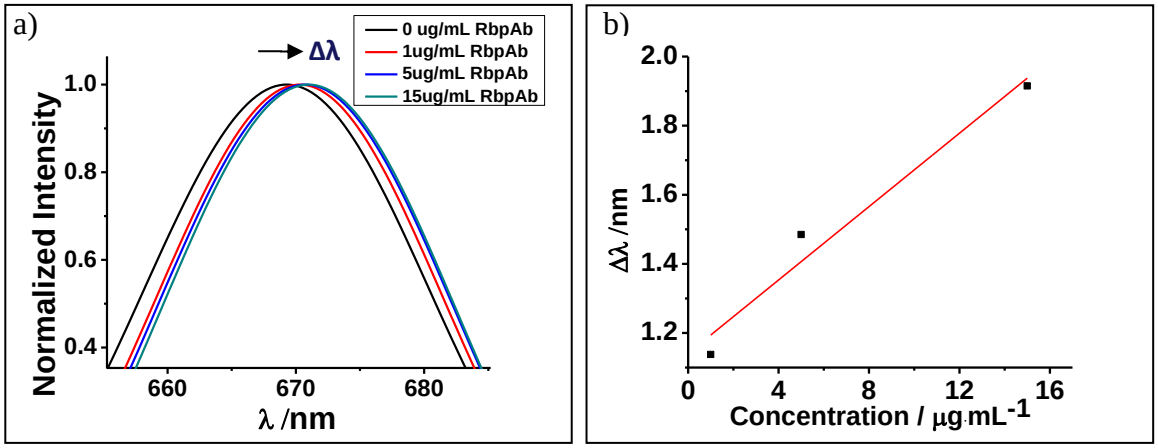

Figure 5-7: (a) Transmission spectrum of one nanohole array after binding of EGFR antibody from solutions of different concentrations ranging from 0 to 15 μg/mL. (b) Linear calibration curve of wavelength shifts of one nanohole array in contact with EGFR antibody solution with different concentrations. The slope of the linear fitted calibration curve was 0.05 nm/μg·mL^{-1}.

A spike and control were also tested for the detection of EGFR antibody experiment in order to ensure the consistency and comparability of the method[79]. We chose bovine serum albumin (BSA), a protein often used as reference or protein concentration standard[80], as the control and spiking solution for the EGFR antibody. The antibody was spiked in 1% BSA in PBS with a final concentration of 1 μg/mL. Figure 5-8 showed that the EGFR antibody spike (1 μg/mL) had a spectral red-shift of 0.6 nm; while the BSA control without EGFR showed insignificant spectrum shift (0.01 nm) comparing to that of the spike. This shift of 0.01 nm was also below the minimum

detectable shift obtained previously (0.09 nm). The results suggested that there were specific adsorption of the antibody to the surface without any binding of BSA. Comparing to the spectral shift of EGFR antibody in PBS (10 μg/mL with $\Delta\lambda$ = 2.2 nm) demonstrated in Figure 5-6, the EGFR spike in BSA had a smaller shift (0.6 nm), which was consistent with its lower concentration (1 μg/mL) where less protein was adsorbed on the surface. However, the expected spectral shift of the EGFR spike was calculated to be 1.2 nm from the linear calibration curve in Figure 5-7(b), which was greater than the actual shift measured (0.6 nm). This inconsistency might be due to the matrix effect, where the surface condition at the interface might not be exactly the same from experiment to experiment, since the calibration was done in the best possible condition in terms of solution composition.

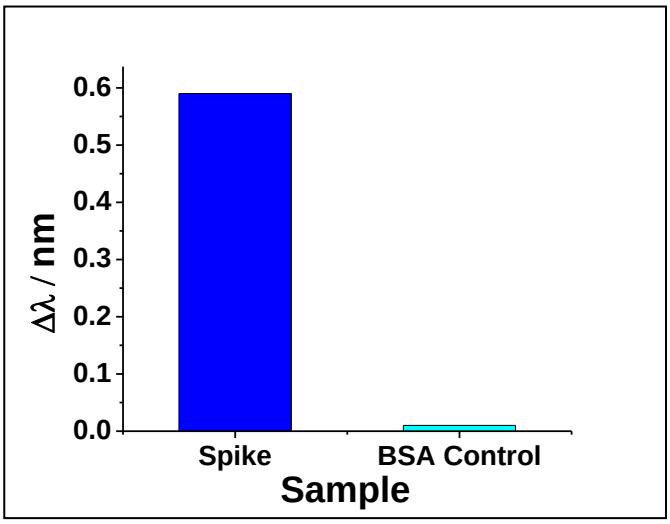

Figure 5-8: Wavelength shifts of the Antibody spiked in 1%BSA and the control. The EGFR antibody was diluted with 1% BSA to a final concentration of 1 μg/mL.

5.2.2.2 Detection of EGFR Antigen

After the development of the method for the detection of EGFR antibody, we decided to move on to detect EGFR antigen, which is more important in terms of biomarker detections[53,54]. As described in section 5.1.2.2, EGFR antibody with a concentration of 10 μg/mL was first immobilized on the surface of the AuFIB samples, and the EGFR antigen (diluted in different solutions with increased medium complexity) was flown through the microfluidic channels. The transmission spectrum after the antibody-antigen interaction was measured. A calibration curve was also generated by monitoring the spectral shift of EGFR antigen solutions diluted in PBS with different concentrations. The error bars in the figures represented the standard deviation calculated for a particular run where the spectrum of four nanohole arrays with the same periodicity were measured and averaged.

In Figure 5-9, a red-shift of 1.2 ± 0.5 nm was observed for the detection of EGFR antigen in PBS (10 μg/mL) suggesting the adsorption of the antigen to the surface[76]. A 1% BSA in PBS was used as a control, and showed insignificant shift (0.04 ± 0.09 nm) comparing to that of the EGFR antigen indicating no unspecific proteins being adsorbed to the surface.

EGFR antigen was then diluted in PBS to different concentrations, ranging from 0 to 10 μg/mL. The transmission spectrum was measured as the EGFR antigen with different concentrations was flowed through the microfluidic channels after the antibody immobilization. An increased red-shift (0.12 ± 0.04 nm to 0.25 ± 0.07 nm) against the spectrum of 0 μg/mL antigen solution was observed as the concentration of the antigen increased from 1 to 10 μg/mL respectively, which suggested more antigens being

absorbed to the surface with the increasing concentration. The averaged spectral shift was plotted against the concentration of EGFR antigen as shown in Figure **5-10.** A linear calibration curve was fitted with a sensitivity (slope) of 1.5 x 10^{-2} nm/μg·mL^{-1}. The detection limit (DL), commonly defined as the minimum concentration or mass of analyte that can be detected, was calculated in this EGFR antigen detection experiment. The DL was determined to be 0.77 μg/mL from three times the standard deviation of the antigen solution.

The EGFR antigen was then spiked in Dulbecco's Modified Eagle Medium (DMEM), a more complex solution as a cell culture containing proteins, vitamins and salts, to a final concentration of 0.5 μg/mL. As demonstrated in Figure 5-11, a red-shift of 0.2 ± 0.1 nm was observed for the EGFR spike in DMEM, and the spectral shift of DMEM control (0.00 ± 0.01 nm) was negligible comparing to that of the spike indicating specific interaction between EGFR antibody and antigen was detected without any unspecific protein adsorptions from the DMEM medium. In comparison with the spectral shift of EGFR antigen in PBS (1.2 nm for 10 μg/mL EGFR), the smaller shift of the spike (0.2 nm) was a result of its lower concentration (0.5 μg/mL) where less proteins being absorbed to the surface[76].

The observed shift in the EGFR spike in DMEM at 0.5 μg/mL experiment was surprising, considering that the concentration was close to the DL obtained from Figure 5-10. We estimated that the spectral shift of the EGFR spike in DMEM should have been lower than 0.12 nm, since the minimum concentration of the EGFR calibration curve (1 μg/mL) had a shift of 0.12 nm. This discrepancy might have been caused by variances between the spike and the calibration measurements, since the two experiments were

done at different times. Different chips were used and the result might illustrate the variations that might be attributed to differences surface chemistry conditions.

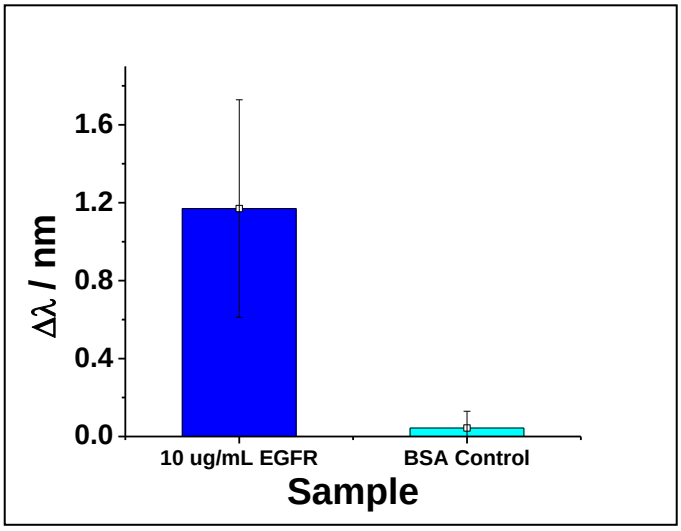

Figure 5-9: Average wavelength shifts of BSA control and EGFR diluted in PBS (10 μg/mL). EGFR antibody (10 μg/mL) was immobilized on AuFIB Sample.

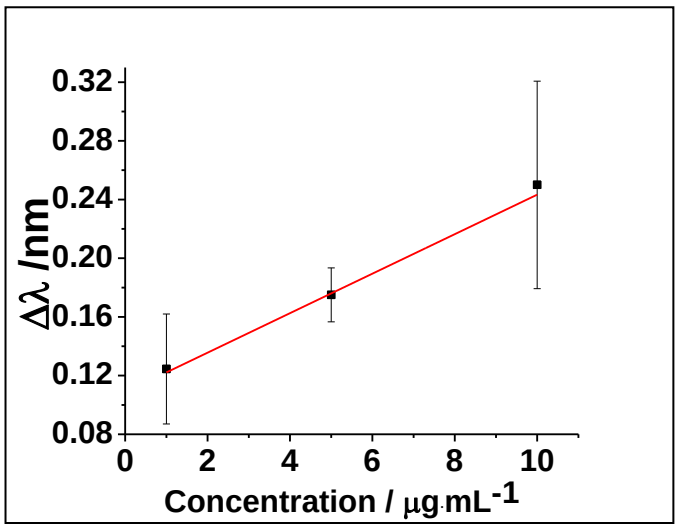

Figure 5-10: Wavelength shifts of nanohole arrays in contact with EGFR antigen solution with different concentrations (0 -10 μg/mL). The slope of the linear fitted calibration curve was 1.3 x 10^{-2} nm/μg·mL^{-1}.

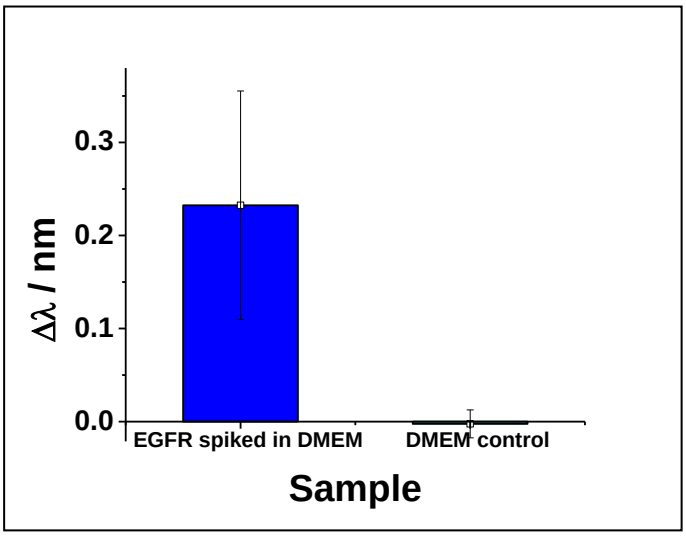

Figure 5-11: Wavelength shifts of EGFR antigen spiked in DMEM and the DMEM control. The final EGFR antigen concentration = 0.5 μg/mL.

5.2.2.3 Detection of EGFR Antigen from Cell Lysates

Detection of EGFR antigen from cells was then performed using the SPR transmission experiment setup. The cells were first harvested and then lysed to release the whole EGFR antigen from the cell membrane (procedure described in section 4.1.2). The prepared EGFR cell lysate solutions were then flowed through the microfluidic channels on top of the nanohole arrays where the EGFR antibody (10 μg/mL) was immobilized. As shown in Figure 5-12, a red-shift of 0.9 ± 0.2 nm was found for the A549 cell lysate, while the H520 cell lysate had almost no shift (0.0 ± 0.1 nm), suggesting EGFR antigen being detected from the A549, but not from the H520 cell lysate. This result agrees with the fact of A549 cell line being EGFR positive while H520 cell line serving as a control with no EGFR expression. Again, because the measured spectral shift of the EGFR antigen in A549 cell was out of the range of the calibration curve obtained in Figure **5-10**, an expected concentration of EGFR antigen in A549 cell cannot be calculated from it.

However we can estimate that the concentration would be much greater than 10 μg/mL, since the maximum shift of the calibration curve (0.25 nm) was much lower than 0.9 nm and it had a concentration of 10 μg/mL.

The concentration of EGFR antigen from the two cell lysates was independently determined using an ELISA kit. As shown in Figure 5-13, an EGFR concentration of 0.604 μg/mL was found from the A549 cell lysate. H520 cell lysate showed signal below the detection limit of ELISA indicating that no EGFR was found.

According to the calibration curve obtained in Figure **5-10**, the estimated EGFR concentration in A549 lysate from the SPR experiment (> 10 μg/mL) was much greater than the ELISA result (0.604 μg/mL). The calibration and the cell lysate detection experiments were performed at different time when the surface chemistry condition might not be exactly the same, which suggested that the concentration of EGFR in A549 cell lysate estimated from the calibration curve might not be accurate or comparable to the ELISA result. More calibration experiments on the cell lysate are needed to solve this problem.

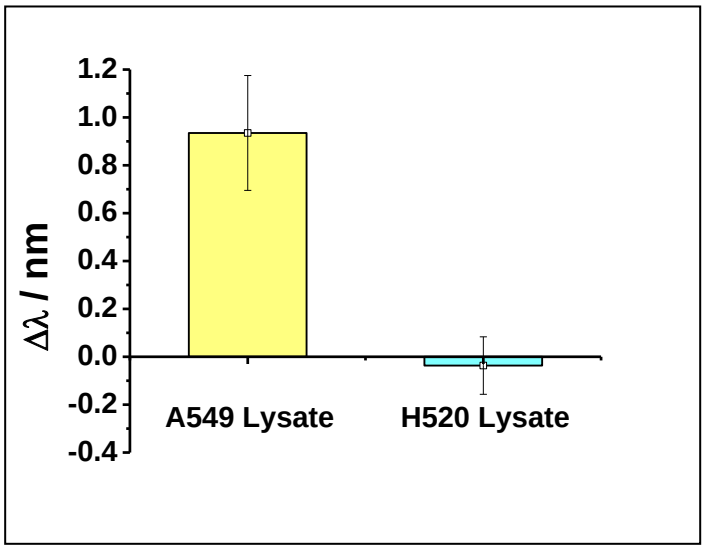

Figure 5-12: Wavelength shifts of A549 (EGFR+) and H520 (EGFR-) cell lysates in contact with the nanohole arrays of AuFIB Sample immobilized with 10 μg/mL EGFR antibody.

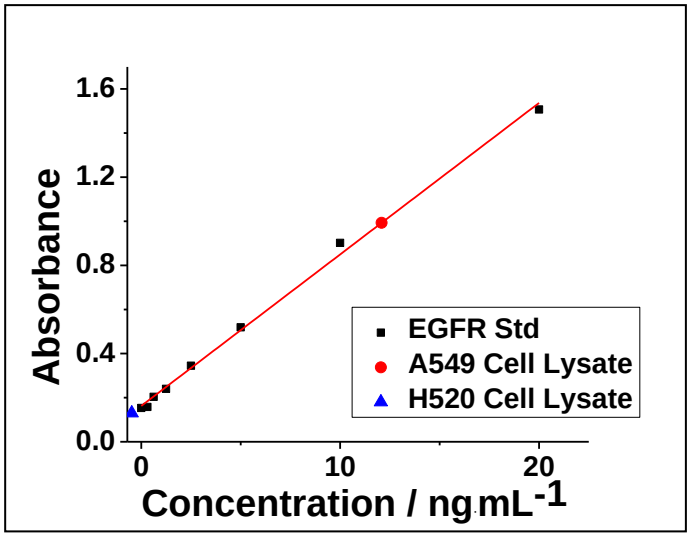

Figure 5-13: The ELISA results of determining the EGFR concentration from A549 and H520 cell lysates. Both the A549 and H520 cell lysates were diluted 50 times for the ELISA. [EGFR antigen in A549] = 604 ng/mL.

5.2.2.4 Summary

A summary of the transmission results for the EGFR antibody and antigen detections was listed in Table 5-1. Overall, the spectral shifts for EGFR antigen detection were smaller than that for the EGFR antibody. The molecular weight of EGFR antigen and antibody are 170 kDa and 180 kDa, respectively[75]. However for the EGFR antigen experiment, EGFR peptide (a fraction of the full EGFR antigen) was used. The peptide fraction (1.38 kDa[81]) has much lower molecular weight and smaller size compared to the EGFR antibody. Therefore the interface refractive index change for the EGFR peptide detection should be smaller than that of the antibody, which justifies a smaller spectral shift[76].

As can be seen from Table 5-1, the measured spectral shifts of the EGFR antibody and antigen spikes were also compared with the expected and the estimated shifts from the linear calibration plots obtained in Figure 5-7(b) and Figure **5-10,** respectively. The difference between the measured and the expected (or estimated) spectral shift of the EGFR antibody and antigen spikes was large (~50% difference both). There might be two explanations for it. Firstly the detection of EGFR antibody or antigen spike was performed in a separated run from the calibration experiments, which might introduce some variations in results such as surface chemistry condition changes from run to run. Secondly we used white light to focus onto the sensor surface (section 4.1.5), which might introduce temperature fluctuations from run to run. A temperature change of 0.1 ℃ during analysis will produce a change in refractive index change (RI) on the order of 1 x 10^{-5} RIU for aqueous solution[82]. Therefore with possible temperature difference between

the spike and the calibration experiments, SPR measurements might vary if RI changes (due to temperature).

As shown in Table 5-2, an estimated concentration of EGFR in A549 cell lysate (> 10 $\mu g\ mL^{-1}$) from the calibration curve of the SPR experiment was much greater than that determined from the ELISA (0.604 $\mu g\ mL^{-1}$). ELISA is a much more reliable standard method for protein quantifications for decades[45]; this huge difference of the SPR detection result from the ELISA might suggest that the calibration experiment of the EGFR antigen detection by SPR was not quite successful, which gave an inaccurate concentration of EGFR in A549 cell lysate. For future works, more runs of calibration experiments should be conducted to obtain a more precise and accurate method to quantify the concentration of EGFR using the SPR method.

Table 5-1: A summary of spectral red-shifts for the detection of EGFR antibody and antigen.

Detection EGFR Antibody		
Concentration of Ab / $\mu g\ mL^{-1}$	**$\Delta\lambda$ / nm**	
10 (in PBS)	2.2	
1 (in BSA)	0.6	measured
1 (in BSA)	1.2	expected based on the Ab calibration curve
Detection EGFR antigen		
Concentration of Ag / $\mu g\ mL^{-1}$	**$\Delta\lambda$ / nm**	
10 (in PBS)	1.1	
0.5 (in DMEM)	0.2	measured
0.5 (in DMEM)	<0.12	estimated based on the Ag calibration curve

Table 5-2: A summary of concentration determined of the EGFR antigen in A549 cell lysate.

Detection of EGFR from A549 Lysate		
Concentration of Ag / μg mL^{-1}	**Δλ / nm**	
>10 (estimated from calibration curve)	0.9	SPR Experiment
0.604	-	ELISA

5.2.3 CD19 and CD20 Detections using Nanohle-SPR Transmission Experiment

With the purpose of developing a practical portable sensor device for cancer diagnosis and cancer subtype classifications, we decided to test if the SPR experiment setup applies to the detection of other biomarker such as CD19 and CD20 antigen for leukemia. From the previous section, we have demonstrated that we were able to detect EGFR in different matrix solutions including in cell lysate. For the CD19 and CD20 antigen detections, we only performed it in cell lysate solution as our final goal. As described in section 4.1.4, after modifying the AuFIB surface with CD19 or CD20 antibody (both 10 μg/mL), a cell lysate solution containing CD19 or CD20 was flowed through the microfluidic channels on top of the modified surface. The binding of either CD19 or CD20 antigens were monitored by measuring the wavelength shift of the white transmitted spectra.

5.2.3.1 Detection of CD19 Antigen

Figure 5-14(a) showed a red-shift of 0.30 ± 0.05 nm for CRL 3000 cell lysate (CD19 positive), indicating CD19 antigen being detected and adsorbed to the surface. The spectrum shift of CCL 155 (CD19 negative) cell lysate was 0.08 ± 0.04 nm, which

was insignificant, since the shift was below the minimum detectable (0.09 nm) by our setup (discussed in section 5.2.1). The concentration of CD19 in CRL 3000 was independently determined to be 0.581 µg/mL form the ELISA calibration curve, shown in Figure 5-14(b).

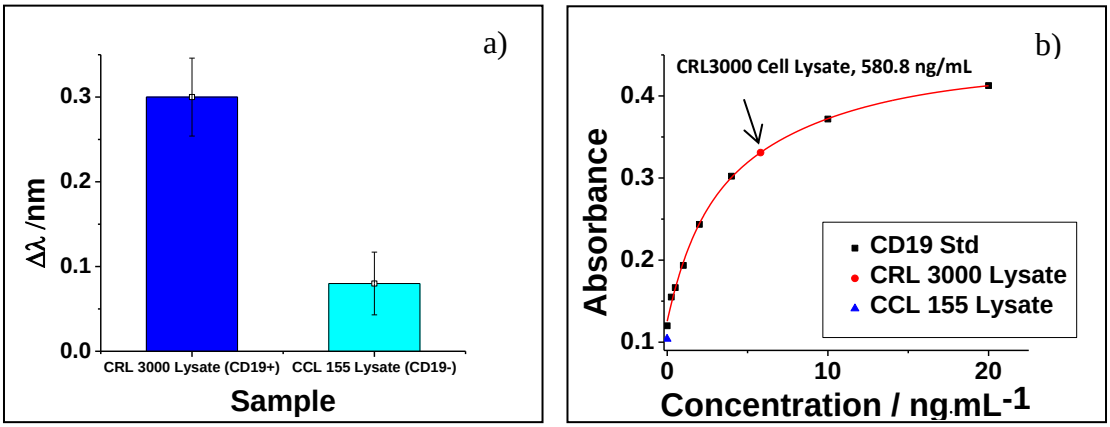

Figure 5-14: (a) Wavelength shifts of CD19 antigens in CRL 3000 and CCL 155 cell lysates in contact with the nanohole arrays of Sample one. (b) Determination of CD19 antigen concentration from the ELISA calibration curve. The concentration of CD19 in CRL 3000 cell lysate = 580.8 ng/mL. Both CRL 3000 and CCL 155 cell lysates were diluted 100 times with PBS.

5.2.3.2 Detection of CD20 Antigen

Red-shifts of 0.8 ± 0.1 nm and 0.1 ± 0.1 nm were observed for the detection of CD20 antigen in CRL 3000 (CD20 positive) and CCL 155 (CD20 negative) cell lysates, respectively, as shown in Figure 5-15(a). The spectral shift for CCL155 cell lysate was slightly above the minimum detectable (0.09 nm), but considered negligible when compared to that of the CRL 3000 cell lysate. This agreed with the fact that CCL 155 was CD20 negative and acted only as a control. The concentration of CD20 antigen in CRL

3000 and CCL 155 cell lysates were independently determined to be 7.001 μg/mL and 1.306 μg/mL respectively from the ELISA calibration curve shown in Figure 5-15(b).

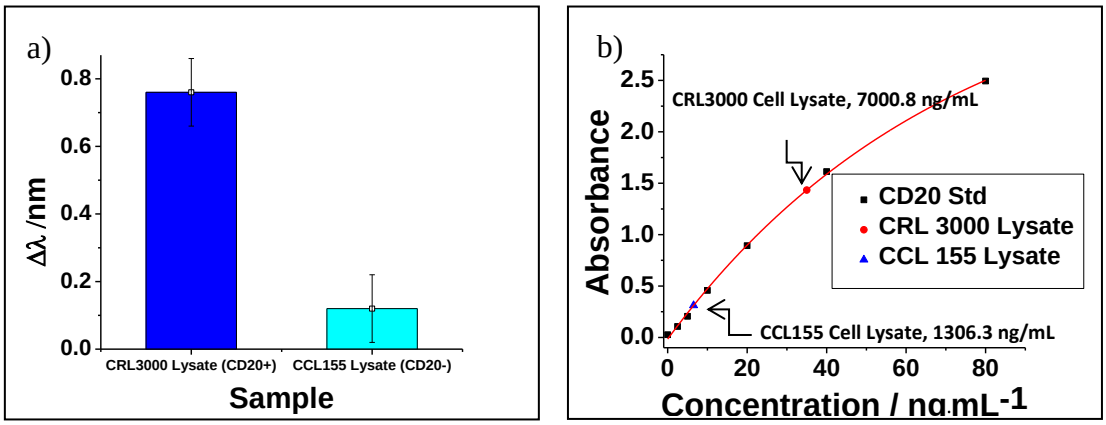

Figure 5-15: (a) Wavelength shifts of CD20 antigens in CRL 3000 and CCL 155 cell lysates in contact with the nanohole arrays of Sample one. (b) Determination of CD20 antigen concentration from ELISA calibration curve. The concentration of CD20 in CRL 3000 lysate = 7000.8 ng/mL. Both CRL 3000 and CCL 155 cell lysates were diluted 200 times with PBS.

5.2.3.3 Summary

Both CD 19 and CD20 antigens were successfully detected from cell lysate solutions using the SPR setup. A summary of the transmission results for the detection of CD19 and CD20 antigens is listed in Table 5-3. A larger spectral shift was found for CD20 due to more proteins being absorbed to the gold surface[76]. This was consistent with a higher concentration determined from ELISA, as shown in Table 5-3. Nevertheless, the concentration of CD20 is about twelve times higher than that of CD19, while its Δλ was only about two times larger than that of CD19. The CD20 antigen being absorbed to the gold surface might have reached saturation, which caused this inconsistent ratio between

the spectral shift and concentration (see section 2.2.3). Also studies have showed that CD19 expression was significantly lower than the amount of CD20 in leukemia[58], which might explain why the concentration of CD20 in CRL 3000 cell line was much higher than that of CD19 determined from ELISA. For future works, SPR calibration experiments should be performed for the CD19 and CD20 antigens detections in order to quantify them using the SPR setup. A kinetic study would also be helpful to determine the maximum shift that we could measure when a saturation point is reached.

Table 5-3: A summary of spectrum red-shifts for the detection of CD19 and CD20 antigens in CRL3000 cell lysate

Detection of CD19 Antigen		***Detection of CD20 Antigen***	
Concentration of Ag / μg mL^{-1}	**Δλ / nm**	**Concentration of Ag / μg mL^{-1}**	**Δλ / nm**
0.581 (in cell lysate)	0.30	7.001 (in cell lysate)	0.76

5.3 Source of Error

As discussed previously, the concentration of EGFR antigen in cell lysate was determined from the calibration curve of the SPR experiment, which was not quite comparable with the ELISA result.

Firstly, although we tried to be consistent with the surface modification, all experiments were not realized on the same day. Variations in surface chemistry, temperature and possible sample-to-sample variance might have introduced inconsistency among measurements. Moreover, the cleaning procedures (i.e. plasma oven) for the AuFIB samples might also damage the nanohole structures on the Au surface over time, which introduced uncertainties among measurements from experiment to experiment.

Secondly, since binding curves were not obtained, differences in incubation times could have introduced inconsistencies between measurements. As mentioned in section 2.2.3, initially the spectral shift, which is proportional to the concentration of molecules adsorbed to the gold surface, changes against time. As shown in Figure 5-16, if the spectral shift is not measured at the same time in the plot, the adsorption would be different with an inconsistent concentration. Ideally, these measurements should always been done after the equilibrium (plateau) has been reached. At higher concentrations, however, the surface concentration of the antigen exceeds the capacity of the surface leading to saturation.

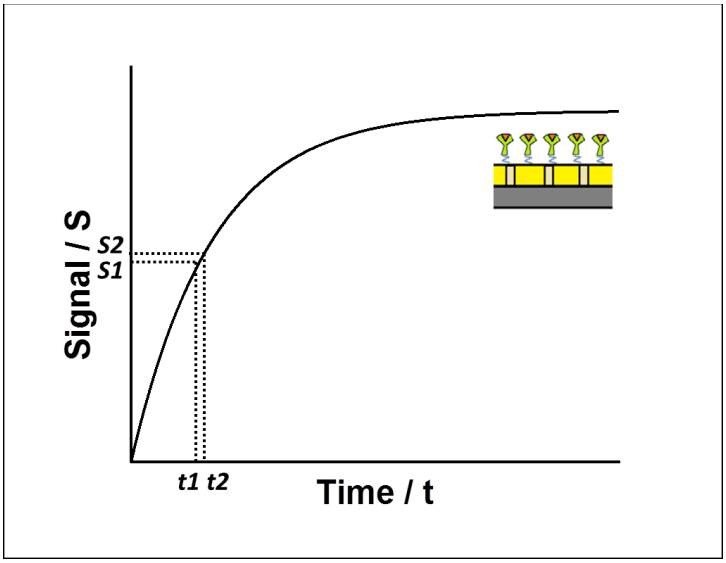

Figure 5-16: Schematic diagram of an affinity kinetic plot of antigen binding to antibody being immobilized on gold surface.

Thirdly, the difference between the diffusion models of the ELISA and the SPR method might also contribute to the variations. The antibody and antigen were introduced in a 96 well polystyrene plate for ELISA. This is a single diffusion model in one

dimension where an antigen solution is left to diffuse over an antibody that is immobilized within a limited space (a well in the polystyrene plate)[45]. On the other hand, the SPR setup coupling with the microfluidic channels allows solutions flowing through a channel, where an antigen solution is continuously flowing over an antibody that is immobilized within the channel. This flow-over setup increases the surface to volume ratio and accelerates the diffusion rate of the antibody solution[35,49]. Diffusion is dependent on the size of the concentration gradient[47]; and two different diffusion models might cause a discrepancy in the values of concentration determined from ELISA and SPR. This is related to possible different time scales to reach equilibrium in both methods due to the distinct diffusion regimes. In order to better understand how diffusion would affect the concentration determination of the SPR experiment, more studies should be done for the microfluidic channel flow-over setup in the future.

Chapter Six : Detection of Whole Cancer Cells by Microscopy Imaging and Nanohole SPR

In this chapter, a method for the detection of whole lung cancer cells that present EGFR overexpression will be presented. By using the AuIL sample with larger area of nanohole arrays, it is possible to capture whole cells and detect them with the SPR setup. Comparing to the detection of biomarkers in chapter five, the whole cell capture experiment is easier to perform without further treatment of the cells. By monitoring the number of captured cells from a nanohole structured gold surface modified with EGFR antibody, a proof-of-concept cell capturing device is presented. The SPR transmission spectra were obtained from the nanohole-structured sample after the cells were captured.

6.1 Introduction

6.1.1 Detection of Cancer Cells by Microscopy Imaging

Cancers are traditionally diagnosed mostly based on the analysis of the morphology of tumor tissue cells. However, these morphologic features are not easy to be detected for early cancer diagnosis[83]. A lot of studies have been done on cancer cell capturing by a planar surface modified with either peptides or antibodies that are specific to surface proteins of the cells[68,84,85]. In Chapter five, we demonstrated a method for possible cancer diagnosis that involves detecting cancer biomarkers from cell lysates using SPR transmission experiments. In this chapter, we used a different concept that involves capturing of the whole lung cancer cells (with overexpression of EGFR membrane protein) using a nanohole-structured surface modified with EGFR antibodies. Since the average cell size is ~ 10 μm, they are large enough to be spotted under a regular

optical microscope[47]. The captured cells were then directly counted using optical microscopy images. By comparing the imaging results with control samples, the specific capture of cancer cells with overexpression of EGFR was achieved.

6.1.2 SPR Detections with Plasmonic Nanohole Recorded by Interference Lithography

SPR transmission spectra were also recorded (in air) for the captured cells. The total area of the AuFIB samples (used for the experiments in Chapter five) was only ~ 15 x 15 μm^2. Due to the nature of the cell capturing mechanism, there is a low probability that a ~ 10 μm cell will be perfectly captured right on top of such a small area arrays. In order to overcome this problem, AuIL samples, fabricated by interference lithography (IL) and described in Chapter three, was used for the whole cell experiments. AuIL samples were fabricated by double exposure to two-beam interference patterns (90 degrees to each other), and had an array area of ~ 2 x 2 cm^2. In this case, transmission spectrum can be obtained anywhere within the 2 x 2 cm^2, including anyplace where there was a captured cell. Compared to samples fabricated by FIB, the spatial variation of the sample fabricated by IL is not significant, and this method is then a good alternative for biosensing applications[68].

6.2 Results and Discussion

6.2.1 Cell Detection with Microscopy Imaging

After modifying the AuIL samples with the EGFR antibody (10 μg/mL, procedure described in section 4.1.4), 1 mL of a cell suspension in medium was added to

the sample for 45 minutes following the procedure described in section 4.2.3. The sample was examined in air under the microscope at various locations before and after the incubation with the cells. The number of adsorbed cells was counted within an area of 4 mm^2.

As can be seen from the optical microscopy images of Figure 6-1(b) to (d), after incubation with the A549 cells (a cell line that overexpresses EGFR on the cell surface) to the pre-modified sample, the captured cells could be clearly seen and were well distributed as single cells absorbed on the surface. A number of 44 ± 7 cells within an area of 4 mm^2 (or 11 ± 2 cells/mm^2) was determined. Figure 6-1(a) showed an image of the sample before incubation with the cells for comparison.

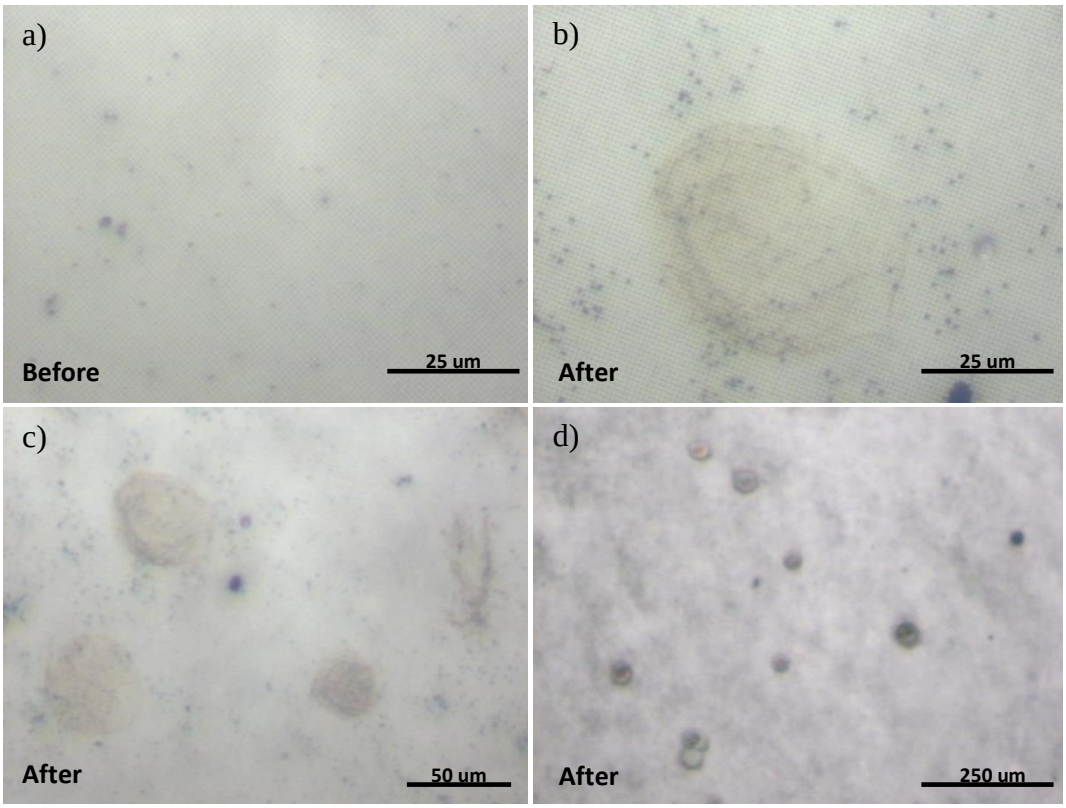

Figure 6-1: (a) Microscopy image of AuIL sample modified with EGFR antibody (10 μg/mL) before incubation with the A549 cells. (b-d) Microscopy images of AuIL sample at different magnifications after A549 cells were captured by the modified surface.

As a control experiment, a suspension of H520 cells, which is EGFR negative, was also incubated with the AuIL sample modified with EGFR antibody (10 μg/mL). As shown in Figure 6-2, although there were a few H520 cells spotted on the pre-modified surface (21 ± 7 cells within an area of 4 mm^2), the overall density of the cell was much lower comparing to that of A549. However the number of cells counted in this experiment provides a background of non-specific cell binding to the surface.

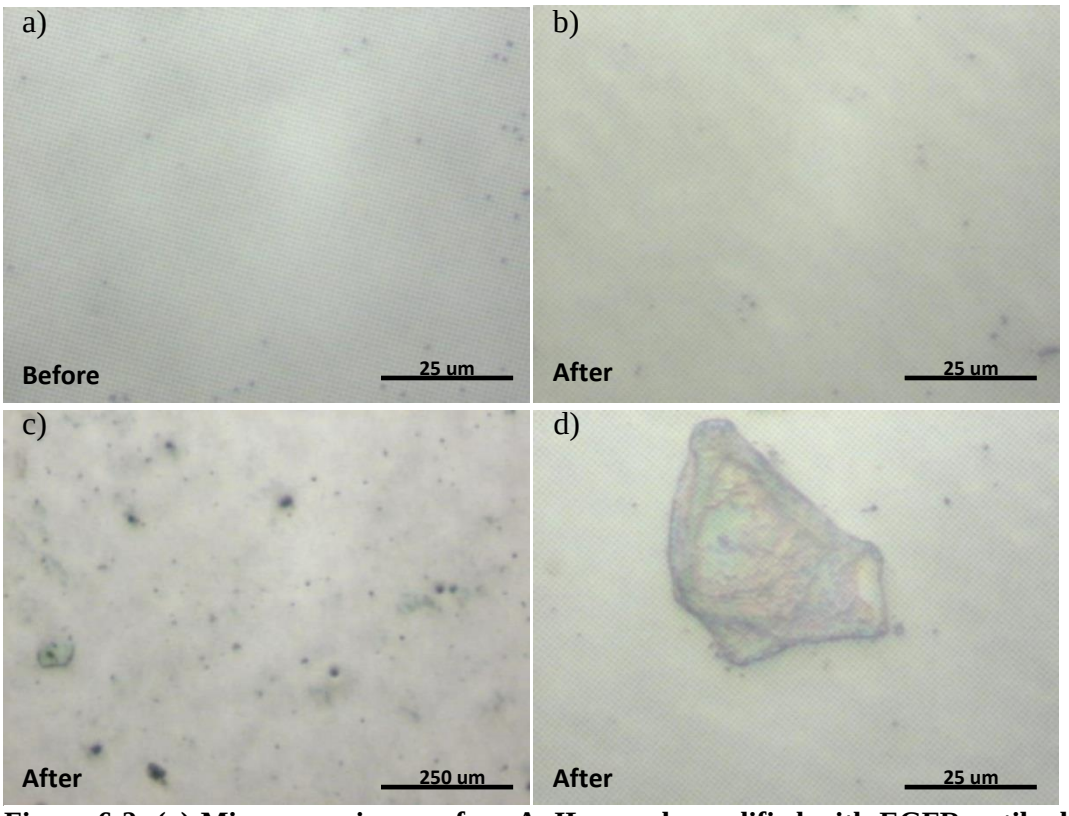

Figure 6-2: (a) Microscope image of an AuIL sample modified with EGFR antibody (10 μg/mL) before incubation with H520 cells. (b-d) Microscopy images of an AuIL sample at different magnifications after incubation with H520 cells.

Two kinds of controls were also included to show the effect of nonspecific cell binding. Both an AuIL sample and a commercially purchased Au-coated glass slides (Evaporated Metal Films, USA) (same type of slides used for the AuFIB fabrication) were incubated with thio-PEG polymer (200 μM) overnight, without adding any EGFR antibody. A monolayer of PEG polymer on gold surfaces is known to reduce nonspecific adsorption of biological molecules by acting as a blocking agent[86]. This should reduce the nonspecific adsorption of A549 or H520 cells during incubation. The number of cells on the surfaces (of both the PEG-modified AuFIB and Au-coated glass slide) was counted, as described above. A summary of all the controls is listed below in Table 6-1.

Table 6-1: Description of Samples Prepared for the Cell Capture Experiment.

Sample	Sample Substrate	Surface Modification	Type of Cell incubated
A549	AuIL, large area of nanohole fabricated by IL	PEG + EGFR Antibody	A549
H520 (control)	AuIL, large area of nanohole fabricated by IL	PEG + EGFR Antibody	H520
A1 (control)	AuIL, large area of nanohole fabricated by IL	PEG	A549
H1 (control)	AuIL, large area of nanohole fabricated by IL	PEG	H520
A2 (control)	commercially purchased glass slides coated with 100nm Au	PEG	A549
H2 (control)	commercially purchased glass slides coated with 100 nm Au	PEG	H520

Controls A1 and H1 involved AuIL as the substrate for capturing the cells, and these samples were incubated on cell suspensions of A549 and H520, respectively. As can be seen from the figures below, both controls, A1 (Figure 6-3) and H1 (Figure 6-4), did not have significant amount of cells absorbed to their surfaces compared to that of

A549. The A549 and H520 cells captured from A1 and H1 were determined to be 21 ± 4 and 17 ± 5 within an area of 4 mm^2, respectively. The amount of cells detected was significantly less than that of A549, indicating a reduced cell- specific binding to the surface.

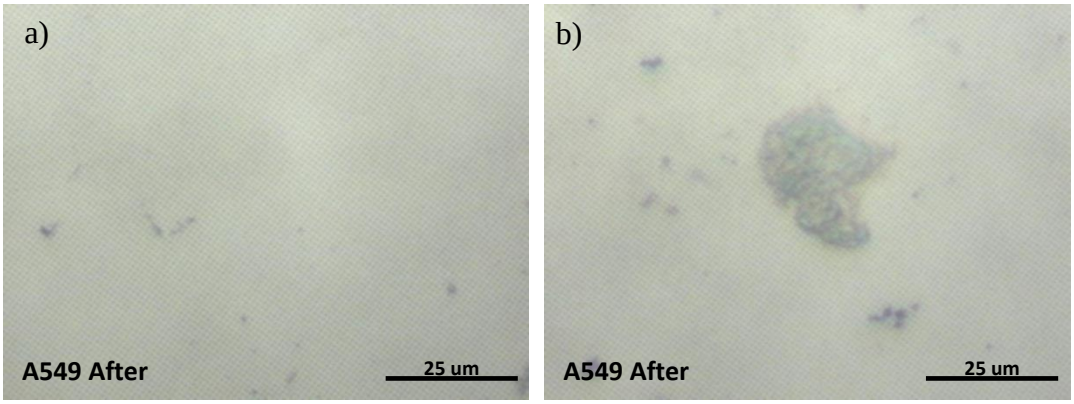

Figure 6-3: (a-b) Microscopy images of AuIL (control A1) modified with thio-PEG after addition of A549 cells.

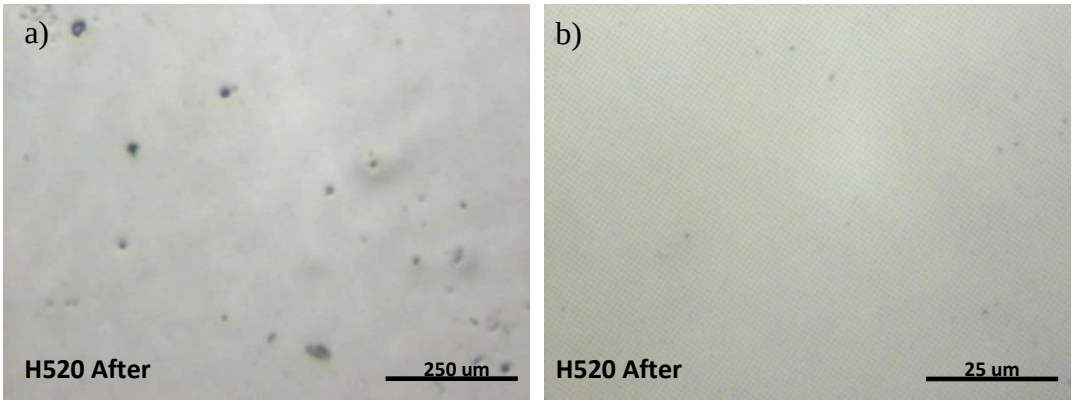

Figure 6-4: (a-b) Microscopy images of AuIL (control H1) modified with thio-PEG after addition of H520 cells.

After modification with PEG polymer, the same amounts of A549 and H520 cell suspensions were added to the controls A2 and H2, respectively. Figure 6-5 presents the images of the controls after incubation with the cells. The number of cells captured by A2 and H2 was determined to be 23 $\pm$ 5 and 22 $\pm$ 5, within an area of 4 mm^2. Both A2 and H2, again, showed a smaller number of cells captured, when compared to that of A549. This suggests some degree of unspecific cell bindings to the surface.

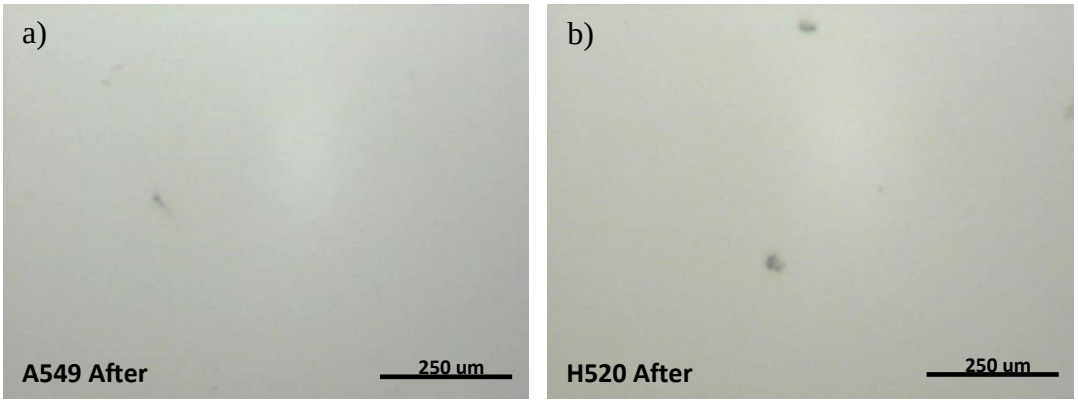

Figure 6-5: Microscopy image of A2 using commercially purchased glass slide after addition of A549 cells (a). Microscopy image of H2 using commercially purchased glass slide after addition of H520 cells (b).

A summary of the number of cells being captured on each of the sample is included in Figure 6-6. The number of A549 cells being captured on AuIL (modified with EGFR antibody) was about twice than that of the H520 cells and the rest of the controls, indicating the specific binding between A549 cells and EGFR antibody being identified. Even though the controls had some cells being captured, the number was constant among them and likely represented the level of background from nonspecific interactions.

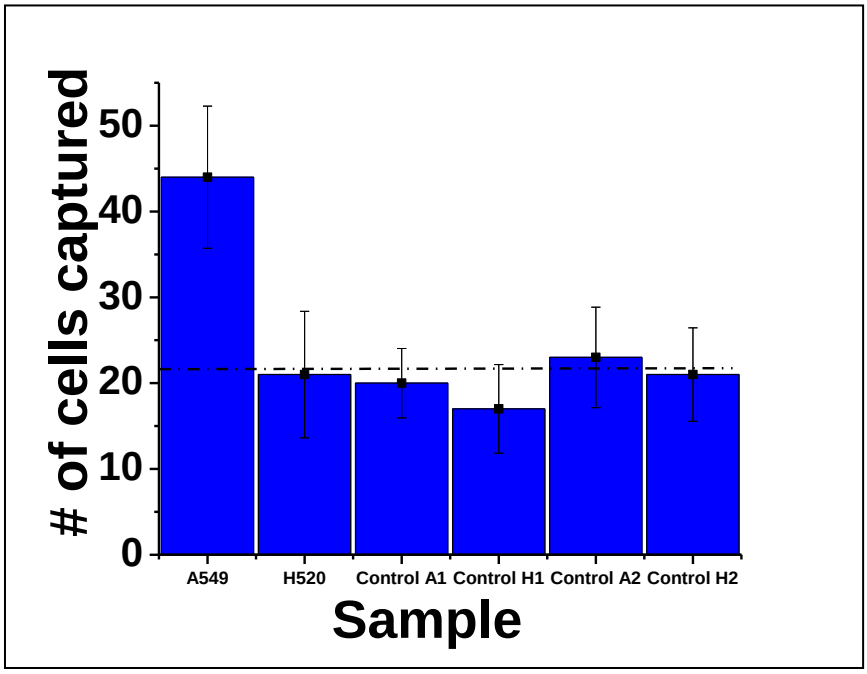

Figure 6-6: A summary plot of the number of cells captured on controls and AuIL after addition of A549 and H520 cells.

6.2.2 A549 Cell Detection using Nanohole SPR Transmission Experiment

A transmission spectrum through the nanoholes was recorded in air for the AuIL sample (modified with EGFR Ab) before and after the cell capture. The spectral shift was determined using the same SPR transmission method explained in section 4.1.6. Figure 6-7 illustrated the average spectral shifts for AuIL obtained from four different locations of the sample, some of them containing cells and some others without cells. An average red-shift of 2.0 ± 0.3 nm was found when there was a cell captured on the surface; while the spectral shift in regions without cells was insignificant (0.1 ± 0.5 nm). This result further confirmed the cell binding to the surface due to the refractive index change at the interface of the sample[76]. Although microscopy imaging seems an easy approach to

determine if there is cell binging to the surface by simply looking by eyes, SPR transmission experiment has some advantages such as providing quantitative measurements that is more objective. It could also be used for SPR mapping by acquiring data to be visualized in the form of a refractive index map[87], which might be less time consuming comparing to counting cells one by one using a microscope. Besides, a portable SPR sensor device could be more practical when microscope is not available.

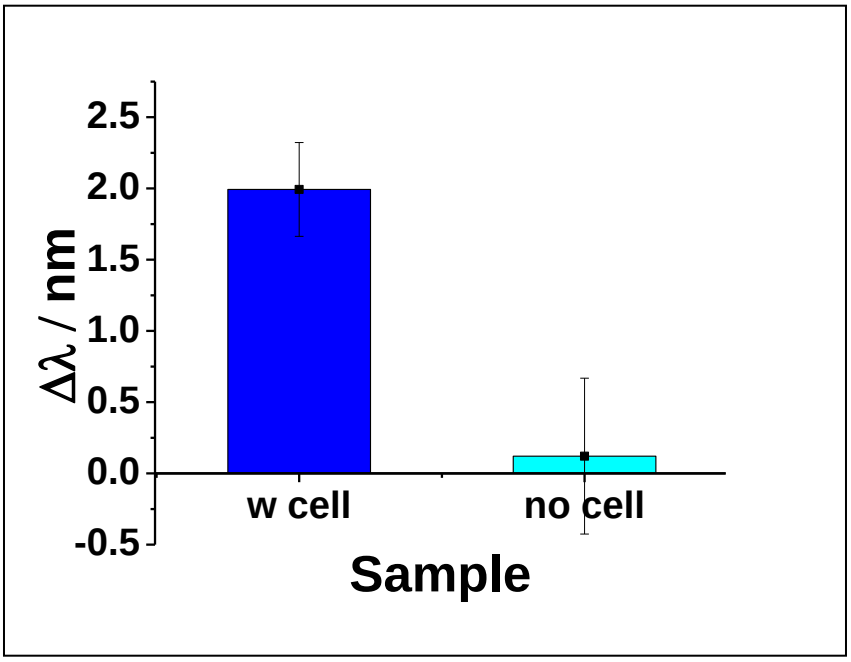

Figure 6-7: Average wavelength shifts at the interface of AuIL with nanohole arrays when there was or not a cell detected by the microscopy image.

6.2.3 Summary

A method for cell-type-specific capture on a modified surface, coupled with SPR transmission detection, was demonstrated in this chapter. The density of captured A549

cells specific to EGFR antibody was determined to be 11 ± 2 cells/mm^2. The results were promising. It is worth to note that the control samples showed some non-specific cell binding to the surfaces; but by modifying the surface with PEG monolayer (to prevent non-specific adsorption)[86], the non-specific background was kept constant and consistent among the controls. The use of AuIL, a large area arrangement of nanoholes fabricated by interference lithography, showed a possibly alternative for label-free biosensing by whole cell capture. Even though the reusability of AuIL was limited due to its fragility during cleaning, the fabrication method is inexpensive and less time-consuming compared to the other nanofabrication method such as FIB and e-beam lithography[88]. This suggests that the interference lithography fabrication methodology has a good potential for the mass production of plasmonic platforms for biosensing.

Chapter Seven : Conclusions

7.1 Conclusions

In this thesis, we have successfully demonstrated the detection of different biomarkers using the SPR setup based on EOT with nanohole arrays on gold surface. The concentration of the EGFR biomarker in cell lysate was determined using the SPR setup and compared with the ELISA result. A whole cell capture experiment using microscopy imaging was also conducted using A549 lung cancer cells with a gold sensor sample fabricated by interference lithography. The result was further confirmed by the SPR setup. A summary of the results is listed in Table 7-1.

A concentration of >10 μg/mL was estimated for the EGFR in A549 cell lysate using the SPR setup, which is much higher than that from the ELISA analysis. This difference between the ELISA and SPR results was explained with a few possibilities in section 5.3. Surface chemistry, cleaning procedures, difference in binding kinetics and possible temperature variations might introduce inconsistent measurements from run to run, which can result an inaccurate calibration determined for the SPR method. Moreover, different diffusion models, which lead to possible different time scale to reach equilibrium in both methods, might cause the discrepancy in the determination of EGFR concentration between the ELISA and the SPR methods.

By microscopy imaging, a number of 11 ± 2 cells/mm^2 of A549 cells (EGFR positive) was found being captured on a gold sample modified with EGFR antibody. This demonstrated another possible method for cancer diagnosis. A SPR transmission

experiment was also performed further confirmed the cell capture by obtained a spectral shift of 2.0 ± 0.3 nm.

Table 7-1: Summary table of the SPR and the whole cell capture experiment

EGFR in cell lysate	**Concentration**	
From SPR setup	>10 μg/mL	
From ELISA	0.604 μg/mL	
Whole cell capture experiment	**Number of cell captured**	**Δλ from SPR experiment**
A549 Lung cancer cells (EGFR +)	11 ± 2 cells/mm^2	2.0 ± 0.3 nm

7.2 Future Work

The use of SPR instruments has been widely studied for the detection of biological and chemical species[42]. This thesis has successfully demonstrated the detection of different cancer biomarkers using a SPR setup. Kinetic studies should be performed in the future to determine the saturation point of the experiments. Further validation of the calibration and more data collections are also needed in order to improve the accuracy of the method. Reproducibility is an important factor to consider for development of diagnostic devices. For future work, using different surface modification method such as applying polymer films by spin coating[89] instead of self-assembled monolayer method might provide a more consistent surface environment and be helpful to improve the run-to-run variations. There are still some problems need to be overcome for the AuIL sample fabricated by interference lithography. But if it is possible to use the cheaper and disposable AuIL sample for the detection of biomarkers using SPR, the reproducibility might be improved since cleaning and reusing samples would not be a problem anymore.

Interference lithography is commonly used for the fabrication of nanostructure materials for optical applications[66,90,91]. The advantage of generating large area structured patterns using IL made it a good candidate for our whole cell capture experiment. An improvement of the fabrication process such as cleaning step and the adhesion ability of the gold structure to the glass would provide further improvement of the cell capture procedure. Alternately, using different surface immobilization method on the IL sample with different materials (e.g. lipid bilayers, aptamer or streptavidin-biotin)[38,84,92] could be another approach. SPR imaging has been recently published for specific capture of cells, where light intensity or refractive index changes due to cell adsorptions to the sensor were mapped with multiple biomarkers at the same time[77,87,93]. By combining with PDMS microfluidic channels[84], detection of whole cells captured on gold sample in real time with SPR imaging could be a suitable extension from this thesis.

Bibliography

(1) Canadian Cancer Society's Steering Committee on Cancer Statistics. *Canadian Cancer Statistics 2012*; Canadian Cancer Society, Toronto, 2012.

(2) Perez-Diez, A.; Morgun, A.; Shulzhenko, N. *Advances in Experimental Medicine and Biology* **2007,** *593*, 74-85.

(3) Ekerdt, D. J. *Encyclopedia of Aging*; Macmillan Reference USA: New York, 2002.

(4) Dean, M. *Cancer Research* **1998**, *58*, 5633-5636.

(5) Khandurina, J.; Guttman, A. *Journal of chromatography* **2002**, *943*, 159-183.

(6) Sinton, D.; Gordon, R.; Brolo, A. G. *Microfluidics and Nanofluidics* **2008**, *4*, 107-116.

(7) Siegel, R.; Naishadham, D.; Jemal, A. *CA: A Cancer Journal for Clinicians* **2012**, *62*, 10-29.

(8) Cancer Research UK. *World Cancer Factsheet.* Retrieved November 21, 2012, from http://www.cancerresearchuk.org

(9) Haskell, C. M.; Berek, J. S. *Cancer Treatment*; 5th ed.; W.B. Saunders: Philadelphia, 2001.

(10) Matini, N. (1982). *Recent Results in Cancer Research* **1982,** *82*, 174-178.

(11) Heath, M. E.; Cheson, B. D. *American Journal of Hematology* **1985,** *19*, 63-73.

(12) Boggs, D. R.; Sofferman, S. A.; Wintrobe, M. M.; Cartwright, G. E. *American Journal of Medicine* **1966,** *40*, 243-254.

(13) Henderson, E. S.; Lister, T. A.; Greaves, M. F. *Leukemia;* W.B. Saunders: Philadelphia, 2002.

(14) St. John, T. M. *With every breath: A lung cancer guidebook*; Vancouver, 2003.

(15) Melamed, M. R.; Flehinger, B. J.; Zaman, M. B.; Heelan, R. T.; Perchick, W. A.; Martini, N. *Chest* **1984**, *86*, 44-53.

(16) Murray, K. L.; Duvall, E.; Salter, D. M.; Monaghan, H. *Cytopathology* **2002**, *13*, 350.

(17) Rangdaeng, S.; Ya-In, C.; Settakorn, J.; Chaiwun, B.; Bhothirat, C.; Sirvanichai, C.; Aramratana, A. *Journal of the medical association of Thailand* **2002**, *85*, 953.

(18) Tsukuda, S.; Heshiki, A.; Katsuragawa, S.; Li, Q.; MacMahon, H.; Doi, K. (2002). *Radiology* **2002**, *223*, 199.

(19) Humphrey, L. L.; Teutsch, S.; Johnson, M. *Annals of Internal Medicine* **2004**, *140*, 740-753.

(20) Speicher, M. R.; Gwyn, B. S.; Ward, D. C. *Nature Genetic* **1996**, *12*, 368-375.

(21) Van Dongen, J. J.; Krissansen, G. W.; Wolvers-Tettero, I. L.; Comans-Bitter, W. M.; Adriaansen, H. J.; Hooijkaas, H.; van Wering, E. R.; Terhorst, C. *Blood* **1988**, *71*, 603-612.

(22) Jennings, C. D.; Foon, K. A. *Cancer Investigation* **1997**, *15*, 384-399.

(23) Bermard, A.; Boumsell, L.; Dausset, J.; Milstein, C.; Schlossman, S. F. *Leucocyte Typing*; Springer Verlag: Berlin, 1984.

(24) Schwab, M. *Encyclopedic Reference of Cancer*; Springer: Heidelberg, 2001.

(25) Bunn, P. A.; Helfrich, B.; Soriano, A. F.; Franklin, W. A.; Varella-Garcia, M.; Hirsch, F. R.; Baron, A.; Zeng, C.; Chan, D.C. *Clinical Cancer Research* **2001**, *7*, 3239-3250.
(26) Silvestri, G. A. *Chest* **2005**, *128*, 3975-3984.
(27) Wood R.W. *Philosophical Magazine* **1902**, *4*, 396-402.
(28) Fano, U. *Journal of the Optical Society of America* **1941**, *31*, 213-222.
(29) Pines, D. *Reviews of Modern Physics*, **1956**, *28*, 184-198.
(30) Ritchie, R. H. *Physical Review*, **1957**, *106*, 874-881.
(31) Ritchie, T. H.; Arakawa, E. T.; Cowan, J.J.; Hamm, R.N. *Physical Reviews*, **1968**, *21*, 1530–1532.
(32) Kretschmann, E.; Raether, H. *Zeitschrift fuer Naturforschung. Teil A, Astrophysik, Physik und physikalische Chemie*, **1968**, *A23***,** 2135-2136.
(33) Kretschmann, E. *Optics Communications*, **1972**, *5*, 331-336.
(34) Gwon, H. R.; Lee, S. H. *Materials Transactions*, **2010**, *51*, 1150-1155.
(35) www.biocore.com
(36) Abbas, A.; Linman, M. J.; Cheng, Q. (2011). *Biosensors and Bioelectronics*, **2011**, *26*, 1815-1824.
(37) Barnes, W.; Dereux, A.; Ebbesen, T. W. *Nature*, **2003**, *424*, 824-830.
(38) Homola, J.; Yee, S. S.; Gauglitz, G. (1999). *Sensors and Actuators.B: Chemical*, **1999**, *54*, 3-15.
(39) Raether, H. *Surface Plasmons on Smooth and Rough Surfaces and on Gratings;* Springer-Verlag: New York, 1986.
(40) De Feijter, J.A.; Benjamins J.; Veer, F.A. Biopolymers, 1978, 17, 1759-1772.
(41) Ordal, M. A.; Long, L. L.; Bell, R. J.; Bell, S. E.; Bell, R. R.; Alexander, R. W.; Ward, C. A. *Applied Optics*, **1983**, *22*, 1099-1119.
(42) Homola, J. *Surface Plasmon Resonance Based Sensors*; Springer-Verlag: New York, 2006.
(43) Bethe, H. *Physical Review*, **1944**, *66*, 163-182.
(44) Nijkamp, F. P.; Parnham, M. J. *Principles of Immunopharmacology*; 3 ed; BirkhaIuser Verlag: Basel, 2011.
(45) Butler, J. E. *Journal of immunoassay*, **2000**, *21*, 165-209.
(46) Engvall, E.; Perlmann, P. *Immunochemistry*, **1971,** *8*, 871-874.
(47) Nelson, D. L.; Lehninger, A. L.; Cox, M. M. *Lehninger Principles of Biochemistry*; 5 ed; W. H. Freeman: New York, 2005.
(48) Fernandez, F.; Hegnerova, K.; Piliarik, M.; Sanchez-Baeza, F.; Homola, J.; Marco, M. P. et al. *Biosensors and Bioelectronics*, **2010**, *26*, 1231-1238.
(49) Gordon, R.; Brolo, A. G.; Sinton, D.; Kavanagh, K. L. *Laser and Photonics* Reviews, **2010**, *4*, 311-335.
(50) Lin, S.; Lee, A. S.; Lin, C.; Lee, C. *Current Proteomics*, **2006**, *3*, 271-282.
(51) Goldstein, B.; Coombs, D.; He, X.; Pineda, A.G.; Wofsy, C. *Journal of Molecular Recognition*, **1992**, *12*, 293-199.
(52) Bergin, D. A.; Greene, C. M.; Sterchi, E. E.; Kenna, C.; Geraghty, P.; Belaaouaj, A.; Taggart, C. C.; O'Neill, S. J.; McElvaney, N. G. *Journal of Biological Chemistry*, **2008**, *283*, 31736-31744.
(53) Liu, F.; Zhang, J.; Deng, Y.; Wang, D.; Lu, Y.; Yu, X. *Sensors and Actuators*: *B, Chemical*, **2011**, *153*, 398-403.

(54) Rusch, V.; Klimstra, D.; Venkatraman, E.; Pisters, P. W.; Langenfeld, J.; Dmitrovsky, E. *Clinical Cancer Research*, **1997**, *3*, 515-522.
(55) Willey, J. M.; Linda, S.; Chris, W. *Prescott's Microbiology*; 8 ed; McGraw-Hill: New York, 2005.
(56) Bradbury, L. E.; Kansas, G. S.; Levy, S.; Evans, R. L.; Tedder, T. F. (1992). *The Journal of immunology*, **1992** , *149*, 2841-2850.
(57) Kuijpers, T. W.; Bende, R. J.; Baars, P. A.; Grummels, A.; Derks, I. A. M.; Dolman, K. M.; Beaumont, T.; Tedder, T. F.; Van Noesel, C. J. M.; Eldering, E.; Van Lier, R. A. W. *The Journal of Clinical Investigation*, **2010**, *120*, 214-222.
(58) Ginaldi, L., M.; De Martinis, M.; Matutes, E.; Farahat, N.; Morilla. R.; Daniel, C. *Journal of Clinical Pathology*, **1998**, *51*, 364-369.
(59) Ebbesen, T. W.; Lezec, H. J.; Ghaemi, H. F.; Thio, T.; Wolff, P. A. *Nature*, **1998**, *391*, 667-669.
(60) Tanaka, T.; Irisawa, T.; Fujiwara, M.; Gennai, N. *Thin Solid Films*, **2006**, *509*, 113-117.
(61) Bernard, A.; Michel, B.; Delamarche, E. *Analytical chemistry*, **2001**, *73*, 8-12.
(62) Fu, A. Y.; Spence, C.; Scherer, A.; Arnold, F. H.; Quake, S. R. *Nature Biotechnology*, **1999**, *17*, 1109-1111.
(63) Reyes, D. R.; Iossifidis, D.; Auroux, P. A.; Manz, A. *Analytical Chemistry*, **2002**,*74*, 2623-2636.
(64) Ng, J. M. K.; Gitlin, I.; Stroock, A. D.; Whitesides, G. M. *Electrophoresis*, **2002**, *23*, 3461-3473.
(65) Madsen, D. A. *Engineering Drawing and Design;* 2 ed; Delmar: Alberny, 1996.
(66) Menezes, J. W.; Ferreira, J.; Santos, M. J. L.; Cescato, L.; Brolo, A. G. *Advanced Functional Materials*, **2010**, *20*, 3918-3924.
(67) Menezes, J. W.; Cescato, L.; De Carvalho, E. J.; Braga, E. S. *Optics Express*, **2006**, *14*, 8578-8583.
(68) Menezes, J. W.; Barea, L. A. M.; Chillcce, E. F.; Frateschi, N.; Cescato, L. *IEEE Photonics Journal*, **2012**, *4*, 544-551.
(69) Shirtcliffe, N. J.; Aqil, S.; Evans, C.; McHale, G.; Newton, M.; Perry, C. C.; Paul, R.; *Journal of Micromechanics and Microengineering*, ***2004***, *14*, 1384-1389.
(70) Johansen, K.; Svensson, L. *Methods in Molecular Medicine*, **1997**, *13*, 15-28.
(71) Ji, H. *Cold Spring Harbor Protocols*, **2010**, *2010*, 5466.
(72) Prime, K. L.; Whitesides, G. M. *Science*, **1991**, *252*, 1164-1167.
(73) Grabarek, Z.; Gergely, J. *Ananlytical Biochemistry*, **1990**, *185*, 131-135.
(74) Park, T.; Choo, J.; Lee, M.; Kim, Y. S.; Lee, E. K.; Lee, H. S. *Analytical Sciences*, **2004**, *20*, 1255-1258.
(75) Yao, Y.; Wang, G.; Li, Z.; Yan, B.; Guo, Y.; Jiang, X.; Xi, Z. *Acta Biochimica et Biophysica Sin*, **2010**, *42*, 763-770.
(76) Krishnan, A.; Thio, T.; Kim, T. J.; Lezec, H. J.; Ebbesen, T. W.; Wolff, P. A.; Pendry, J.; Martin-Moreno, L. Garcia-Vidal, F. J. *Optics Communications*, **2001**, *200*, 1-7.
(77) Lee, S. H.; Lindguist, N. C.; Wittenberg, N. J.; Jordan, L. R.; Oh, S. H. Lap on a Chip, 2012, 12, 3882-3890.

(78) Jung, L. S.; Nelson, K. E.; Campbell, C. T.; Stayton, P. S.; Yee, S. S.; Perez-Luna, V.; Lopez, G. P. *Sensors and Actuators B: Chemical*, **1999**, *54*, 137-144.
(79) Dewey, D. J. *Analyst*, **1979**, *104*, 290-298.
(80) Lundblad, R. L. *Application of Solution Protein Chemistry to* Biotechnology; CRC Press: New York, 2009.
(81) Coussens, L.; Van Beveren, C.; Smith, D.; Chen, E.; Mitchell, R. L.; Isacke, C. M.; Verma, I. M.; Ullrich, A. Nature, 1986, 320, 277-280.
(82) Naimushin, A. N.; Soelberg, S. D.; Bartholomew, D. U.; Elkind, J. L.; Furlong, C. E. *Sensors and Actuators*, **2003**, *96*, 253-260.
(83) Luo, J.; Isaacs, W. B.; Trent, J. M.; Duggan, D. J. *Cancer Investigation*, **2003**, *21*, 937-949.
(84) Shen, K.; Tsai, J.; Shi, P.; Kam, L. C. *Journal of the American Chemical Society*, **2009**, *131*, 13204-13205.
(85) Acharya, G.; Chang, C.; Savran, C. *Journal of the American Chemical Society*, **2006**, *128*, 3862-3863.
(86) Yoshimoto, K.; Nishio, M.; Sugasawa, H.; Nagasaki, Y. *Journal of the American Chemical Society*, **2010**, *132*, 7982-7989.
(87) Moh, K. J.; Yuan, X. C.; Bu, J.; Zhu, S. W.; Gao, B. Z. *Optic Express*, **2008**, *16*, 20734-20741.
(88) Foquet, M.; Samiee, K. T.; Kong, X.; Chauduri, B. P.; Lundquist, P. M.; Turner, S. W.; Freudenthal, J.; Roitman, D. B. *Journal of Applied Physics*, **2008**, *103*, 034301-1-034301-9.
(89) Gorton, L. *Biosensors and Mordern Biospecific Analytical Techniques*; 1st ed.; Elservier B. V.: Amsterdam, 2005.
(90) Berger, V.; Gauthier-Lafaye, O.; Costard, E. *Journal of Applied Physics*, **1997**, *82*, 60-64.
(91) Chen, Y. C.; Geddes, J. B.; Iii; Lee, J. T.; Braun, P. V.; Wiltzius, P. *Applied Physics Letters*, **2007**, *91*, 241103-1-241103-3.
(92) Zhang, Z.; Chen, N.; Li, S.; Battig, M. R.; Wang, Y. *Journal of the American Chemical Society*, **2012**, *134*, 15716-15719.
(93) Peelen, D.; Kodoyianni, V.; Lee, J.; Zheng, T.; Shortreed, M. R.; Smith, L. M. *Journal of Proteome Research*, **2006**, *5*, 1580-1585.